Ore Geology Reviews 94 (2018) 414–434

Contents lists available at ScienceDirect

Ore Geology Reviews

journal homepage: www.elsevier.com/locate/oregeorev

Magmatic evolution and W-Sn-U-Nb-Ta mineralization of the Mesozoic Jiulongnao granitic complex, Nanling Range, South China

Na-Xin Guo[a], Zheng Zhao[a,*], Jian-Feng Gao[b], Wei Chen[c], Deng-Hong Wang[a], Yu-Chuan Chen[a]

[a] MLR Key Laboratory of Metallogeny and Mineral Assessment, Institute of Mineral Resources, Chinese Academy of Geological Sciences, Beijing 100037, China
[b] State Key Laboratory of Ore Deposit Geochemistry, Institute of Geochemistry, Chinese Academy of Sciences, Guiyang 550081, China
[c] Geological Survey Party of South Jiangxi Province, Jiangxi Bureau of Geology and Mineral Resources Development, Jiangxi, Ganzhou 341000, China

ARTICLE INFO

Keywords:
Mineralogy
Geochronology
Geochemistry
Jurassic W-dominated deposits
Jiulongnao granitic complex
South China

ABSTRACT

South China is famous for its large-scale mineralization genetically related to widespread Mesozoic granites. The Jiulongnao complex is one of the largest intrusions in southern Jiangxi Province, and is closely associated with W-dominated polymetallic mineralization. The complex comprises four intrusive phases (I-IV). Phase I consists of medium- to coarse-grained, biotite granite, whereas medium- to coarse-grained, porphyritic, biotite granite and muscovite-bearing granite comprise Phase II. Phase III is composed of medium- to fine-grained, porphyritic, biotite granite and Phase IV consists of medium- to fine-grained, garnet- and biotite-bearing granite. These intrusive phases have LA-ICP-MS zircon U-Pb ages of 160.9 ± 0.6 Ma, 158.6 ± 0.7 Ma, 157.0 ± 1.5 Ma and 154.1 ± 1.2 Ma, respectively. All of the granites are enriched in Rb, Th, U, Ta and Pb, and significantly depleted in Eu, Ba, Nb, Sr, P and Ti. They have $\varepsilon_{Hf}(t)$ and $\varepsilon_{Nd}(t)$ values ranging from −17.9 to −8.2, and −10.7 to −9.8, respectively, with two-stage Hf model ages of 1.7–2.3 Ga. They are S-type granites derived by partial melting of Paleo-Proterozoic metasedimentary rocks. The four phases have T_{Zr} of 746–760 °C, 712–802 °C, 798–810 °C, and 648–731 °C, respectively. Oxygen fugacities of Phases I to III display a decreasing trend but Phase IV has much higher oxygen fugacity in its early stage, which decreased in the late stage. The four phases have different accessory mineral assemblages: Phase I is characterized by an assemblage of zircon, apatite, fergusonite, thorite and uraninite, whereas Phase II is rich in thorite, uraninite, REE-bearing minerals (e.g., monazite, fergusonite and xenotime) and fluorite. Monazite is the main accessory mineral in Phase III, whereas Phase IV contains a wide range of minerals, including thorite, uraninite, Nb-Ta-bearing minerals (e.g., fergusonite and pyrochlore), cassiterite and rutile. These mineral assemblages, together with other geological and geochemical features, suggest that W mineralization was genetically related to Phases I, II and IV, whereas U mineralization was most extensive in Phase II. Sn, Nb and Ta mineralization was associated with the highly fractionated of magmas of Phase IV.

1. Introduction

Silicate minerals may record the magmatic evolution of igneous rocks and associated ores. The mineral assemblages and compositions, coupled with whole-rock geochemistry, can be used to study the nature of magma sources and tectonic settings (Wones and Eugster, 1965; Abdel-Rahman and Cuney, 1994; Henry et al., 2005; Yang et al., 2016) and to trace the magmatic evolution (Robinson and Miller, 1999; Wang et al., 2001, 2003; Panina et al., 2017). Mineral chemistry is particularly useful for constraining magmatic and mineralization processes.

South China is famous for the abundance of Mesozoic, large-scale, W-dominated, polymetallic mineralization (Mao et al., 2011; Hu et al., 2017), and the intensive mineralization is closely related to widespread Jurassic granites (Chen et al., 1989; Yin et al., 2002; Li et al., 2004; Zhao et al., 2017a), one of which is the Jiulongnao complex in southern Jiangxi Province. In the Jiulongnao area, vein-type W deposits (e.g., Zhangdongkeng and Meishuping), skarn-type W deposits (e.g., Tianjingwo), greisen-type W deposits (e.g., Hongshuizhai) and hydrothermal U, Nb-Ta and Au-Ag mineralization (e.g., No. 321, Tianjingwo and Shuangba) coexist in, or adjacent to, the Jiulongnao complex (Fig. 2). The mineralization occurred at 151.1–158.3 Ma (Feng et al., 2011a; Guo et al., 2011b; Li et al., 2014; unpublished data of our project). The age of the first phase of the Jiulongnao complex was reported to be 151.1–156.2 Ma (Feng et al., 2011a; Guo et al., 2011a; Wang et al., 2017a,b), but the respective ages of the other phases and the relationship between granites and polymetallic mineralization are

* Corresponding author at: No. 26, Baiwanzhuang Road, Xicheng District, Beijing 100037, China.
E-mail address: kevin8572@hotmail.com (Z. Zhao).

https://doi.org/10.1016/j.oregeorev.2018.02.015
Received 31 December 2017; Received in revised form 9 February 2018; Accepted 10 February 2018
Available online 12 February 2018
0169-1368/

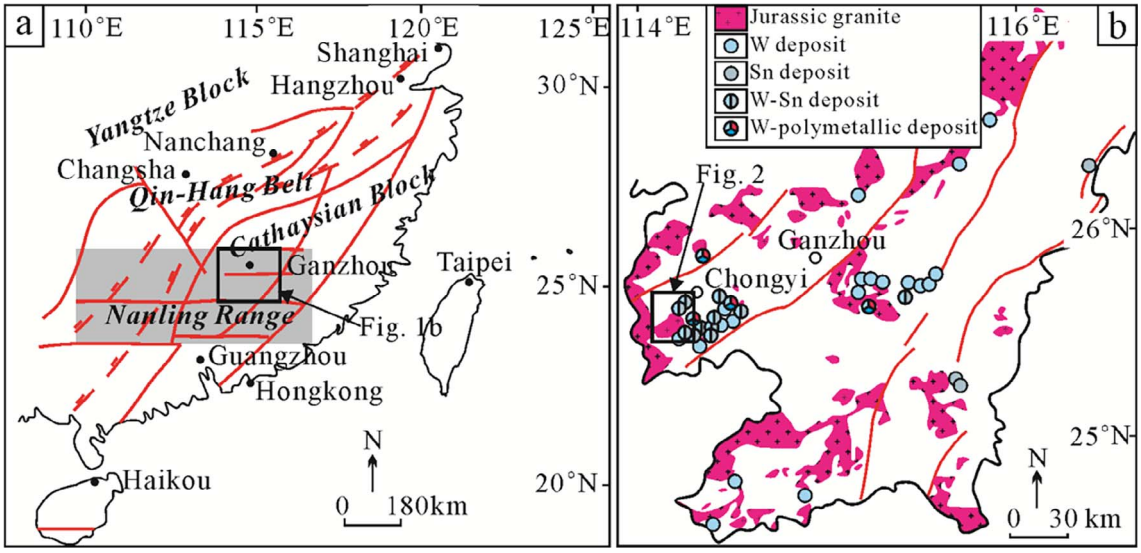

Fig. 1. (a) A schematic tectonic framework of South China; (b) Distribution of Jurassic granites and medium- to large-scale W-Sn deposits in southern Jiangxi Province.

still poorly constrained.

In this contribution, we present the results of a systematic study of the rock-forming and accessory mineral compositions, whole-rock geochemistry and zircon U-Pb dating of the four phases of the Jiulongnao complex. We use these new data to constrain the emplacement ages of the intrusive phases, discriminate the granite types and sources, and address the physicochemical conditions that existed during magmatic evolution. We also present a preliminary discussion of the mineralization processes.

2. Regional geology

The South China Block (SCB) comprises the Yangtze Block in the northwest and the Cathaysian Block in the southeast (Fig. 1a). Extensive Mesozoic felsic magmatism in this region was associated with W, Sn, Mo, Bi, U, Nb, Ta, REE, Cu, Pb and Zn mineralization (Gilder et al., 1991; Zhou and Li, 2000; Mao et al., 2011). The Mesozoic granitic rocks in South China are mostly concentrated in the southeastern part of the region, including Zhejiang, Fujian, Jiangxi, Guangdong and

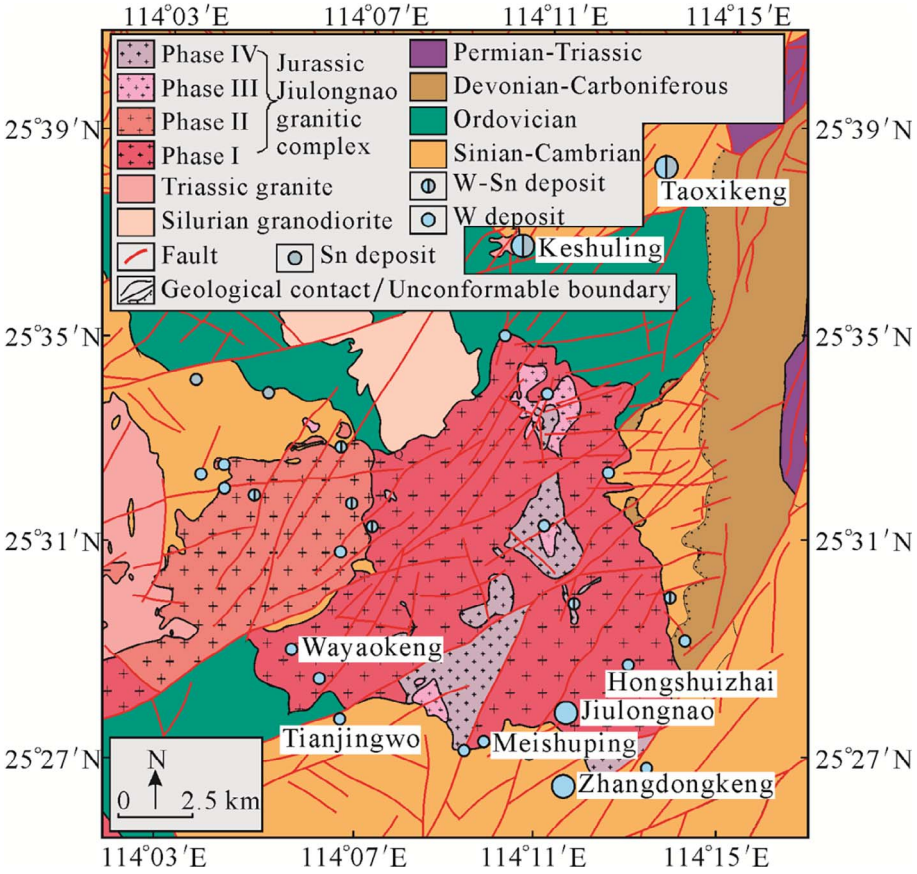

Fig. 2. Geological map of the Jiulongnao complex in southern Jiangxi Province, South China (modified after 1:200,000 geological map and 1:100,000 mining authority map of Chongyi Zhangyuan Tungsten Co., Ltd).

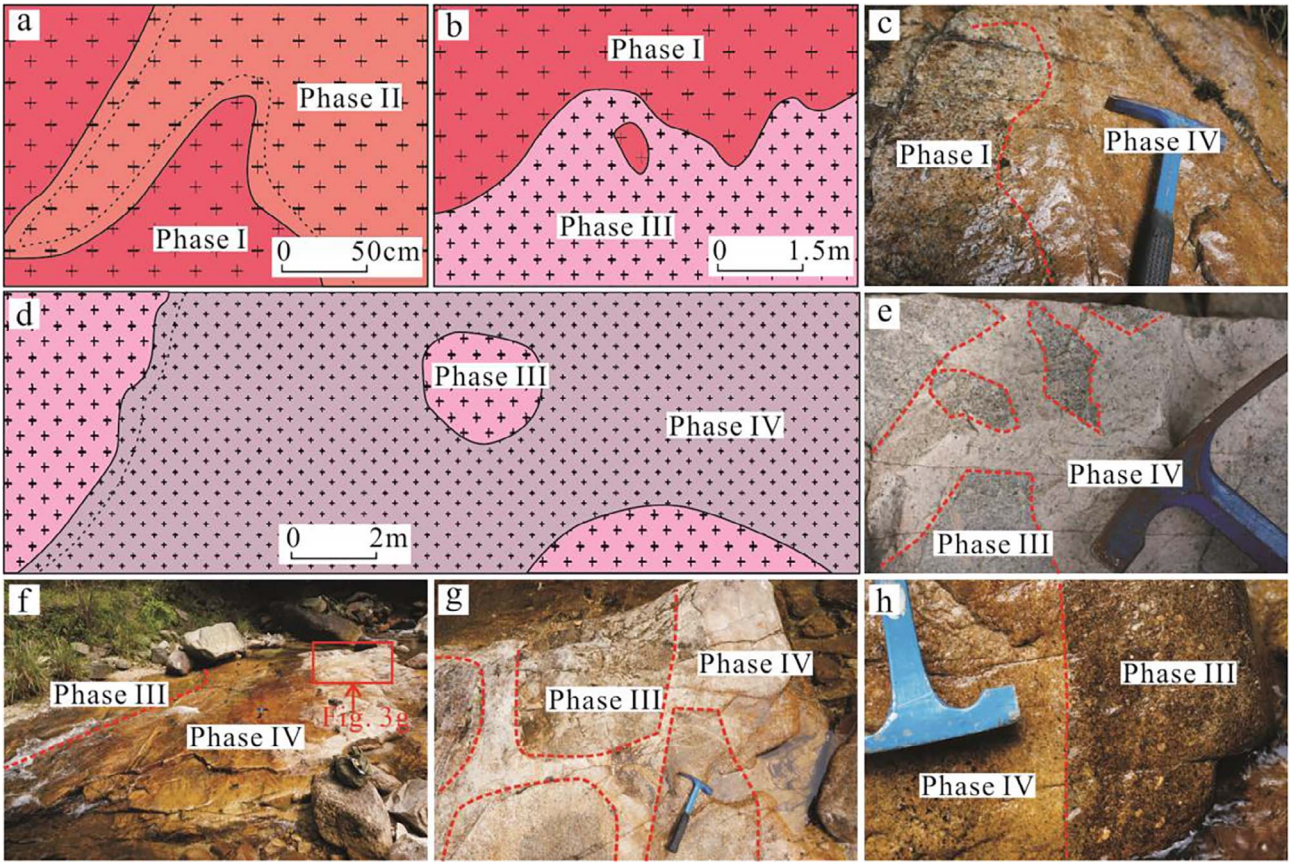

Fig. 3. Contact relations of different phases of the Jiulongnao complex. (a) Phase II intruded Phase I, with a chilled margin in Phase II; (b) Phase III intruded Phase I, with Phase I xenoliths in Phase III; (c) Phase IV intruded Phase I; (d)-(g) Phase IV intruded Phase III, with a chilled margin and Phase III xenoliths in Phase IV; (h) Sharp boundary between Phases III and IV. (a), (b) and (d) from an internal report of Geological Survey Party of South Jiangxi Province.

Hunan provinces, where they have a total outcrop area of ~218,090 km^2. These granites were mainly intruded during two periods, i.e. the Indosinian Period (251–205 Ma) and the Yanshanian Period (180–67 Ma) (Zhou et al., 2006; Faure et al., 2017).

The Nanling Range within the SCB is well known for its extensive Jurassic to Cretaceous magmatic activity, which produced granitic plutons with an aggregate outcrop area of about 64 × 10^3 km^2 (Zhou et al., 2006). The distribution of these plutons was mainly controlled by the Chenxi-Bobai, Changle-Nan'ao and Lishui-Haifeng faults, and they become younger and larger from the northwest to the southeast (Chen et al., 1989; Wang et al., 2007).

In southern Jiangxi Province, multi-stage intrusions are exposed over about 30% of the entire area, and three periods of tectono-magmatism are recognized: the Caledonian Period (Cambrian-Silurian), Indosinian Period (Late Permian-Triassic) and Yanshanian Period (Jurassic-Early Cretaceous). Caledonian granites mainly occur as small intrusions, stocks and sill-like bodies. Indosinian biotite and two-mica granites occur as batholiths and stocks. Yanshanian granites are dominant and occur as complex batholiths, stocks and dykes (Fig. 1b). Emplacement of these granites is controlled by lattice faults with EW-, NS-, NW- and NE-directions. Sedimentary strata in this region are mainly Sinian, Cambrian, Ordovician, Devonian, Carboniferous, Permian, Triassic, Tertiary and Quaternary in age. They are usually divided into three units: (1) A folded basement sequence comprising the Sinian-Cambrian-Ordovician Systems, which is dominated by flysch-like metasandstone and slate, with some lenses of limestone; (2) A folded cover sequence composed of Devonian-Carboniferous-Permian-Triassic clastic and carbonate rocks, with locally interlayered silicalites; and (3) Tertiary-Quaternary Systems consisting of discontinuous sedimentary sequences. The Sinian-Cambrian-Ordovician strata are the main ore-bearing host rocks, containing crevasse- and quartz vein-type, W-Sn deposits and skarn-type Sn-Ag-polymetallic deposits.

The Jiulongnao complex is located in southern Jiangxi Province, in the middle section of the E-W-trending Nanling Range, within the Cathaysian Block. The complex was emplaced into Sinian, Cambrian, Ordovician and Devonian strata, and was controlled by NE-, NW-, NS-, EW- and NNE-trending folds and faults. Granites of later phases commonly intrude earlier phases. Boundaries between the different phases of granites are typically distinct, and marked by rapid changes in lithology (Fig. 3). Chilled margins and xenoliths can be observed in late-phase bodies. On the basis of crosscutting relationships, the Jiulongnao complex can be divided into four phases. Medium- to coarse-grained, biotite granite comprises Phase I. Phase II consists of medium- to coarse-grained, porphyritic, biotite- and muscovite-bearing granite. Phase III is composed of medium- to fine-grained, porphyritic, biotite granite and Phase IV of medium- to fine-grained, garnet- and biotite-bearing granite. Detailed mineralogical and petrographic features of the different granites are summarized in Table 1.

In the Jiulongnao ore field, quartz vein- and greisen-type W deposits and hydrothermal U and Nb-Ta mineralization occur in granitic rocks, whereas quartz vein-type W-Sn deposits occur in the Sinian-Cambrian strata and skarn-type W deposit in Ordovician carbonates (Feng et al., 2011a; Guo et al., 2011a,b; Wang et al., 2016, 2017a,b; Zhao et al., 2017a,b).

Table 1
Lithology and mineralogy of granites in the Jiulongnao complex.

Sample		Lithology	Color	Texture	Rock-forming minerals	Accessory minerals
Phase I	JLN-22 JLN-23 JLN-24 JLN-25	Biotite granite	Gray	Medium- to coarse-grained granitic texture	Quartz (45% ± , anhedral, 4–8 mm), K-feldspar (28% ± , subhedral-snhedral, $3 \times 3\,cm^2$–$2 \times 1\,cm^2$), plagioclase (20% ± , euhedral, $2.5 \times 1\,mm^2$–$5 \times 2\,mm^2$), biotite (7% ± , euhedral-subhedral-anhedral, 2–5 mm)	Zircon, apatite, fergusonite, uraninite
Phase II	DYL601-180-1 DYL601-180-2 DYL801-36-1 DYL801-36-2 DYL801-160-1 DYL801-160-2	Biotie granite Biotite granite	Light salmon-pink Gray	Porphyritic-like texture, medium- to fine-grained texture for groundmass	Phenocrysts: quartz (5% ± , subhedral-anhedral, 5–8 mm), K-feldspar (10% ± , euhedral, $2 \times 0.8\,cm^2$ ±) Groundmass: quartz (30% ± , anhedral, 1–3.5 mm), K-feldspar (35% ± , subhedral, $3.5 \times 3\,mm^2$ ±), plagioclase (13% ± , euhedral, $2.5 \times 1\,mm^2$ ±), biotite (5% ± , eubhedral-anhedral, $1.5 \times 1\,mm^2$–$5 \times 3\,mm^2$), muscovite (2% ± , anhedral)	Zircon, apatite, fluorite, monazite, fergusonite, xenotime, thorite, uraninite
Phase III	JLN-1 JLN-2 JLN-11 JLN-12 JLN-13 JLN-14	Biotie granite	Gray	Porphyritic-like texture, medium- to fine-grained texture for groundmass	Phenocrysts: quartz (1–5%, anhedral, 4–7.5 mm), K-feldspar (10% ± , euhedral, 5–10 mm), plagioclase (2–8%, euhedral, 5–10 mm) Groundmass: quartz (44–50%, subhedral-anhedral, 0.5–2 mm), K-feldspar (15–18%, subhedral-anhedral, $2 \times 1\,mm^2$–$6 \times 4\,mm^2$), plagioclase (13–22%, euhedral-subhedral, $1.5 \times 0.6\,mm^2$–$2.5 \times 2\,mm^2$), biotite (5–7%, subhedral-anhedral, 0.5–2.5 mm)	Zircon, apatite, ilmenite, monazite, allanite, thorite
Phase IV	JLN-6 JLN-7 JLN-8 JLN-15 JLN-16 JLN-17 JLN-18	Garnet- and biotite-bearing biotite granite	Gray	Medium- to fine-grained granitic texture	Quartz (40–50%, subhedral-anhedral, 0.5–2.5 mm), K-feldspar (22–24%, subhedral-anhedral, $1.5 \times 1\,mm^2$), plagioclase (23–30%, euhedral-subhedral, $0.5 \times 0.5\,mm^2$–$2 \times 1.5\,mm^2$), biotite (3–4%, anhedral, 0.5–2 mm), garnet (1% ± , euhedral, 0.3–1.5 mm)	Zircon, apatite, rutile, monazite, fergusonite, xenotime, pyrochlore, uraninite, cassiterite

Table 2
Zircon LA-ICP-MS data for granites of the Jiulongnao complex.

	Spots	Concentrations (ppm)			Th/U	Isotopic ratios						Isotopic Ages (Ma)					
		Pb	Th	U		$^{207}Pb/^{206}Pb$	± σ	$^{207}Pb/^{235}U$	± σ	$^{206}Pb/^{238}U$	± σ	$^{207}Pb/^{206}Pb$	± σ	$^{207}Pb/^{235}U$	± σ	$^{206}Pb/^{238}U$	± σ
Phase I	JLN-22-3	53	472	1864	0.25	0.047344	0.001572	0.163360	0.005084	0.025098	0.000312	64.9	77.8	153.6	4.4	159.8	2
	JLN-22-4	4	58	146	0.39	0.053686	0.007529	0.184655	0.026519	0.024720	0.000840	366.7	325.0	172.1	22.7	157.4	5.3
	JLN-22-6	92	671	3291	0.20	0.048337	0.001243	0.168896	0.004315	0.025371	0.000306	122.3	61.1	158.5	3.7	161.5	1.9
	JLN-22-8	190	1989	6676	0.30	0.051435	0.001193	0.177669	0.003929	0.025060	0.000282	261.2	58.3	166.1	3.4	159.6	1.8
	JLN-22-9	58	628	2021	0.31	0.050107	0.001746	0.173526	0.005967	0.025137	0.000274	198.2	81.5	162.5	5.2	160.0	1.7
	JLN-22-10	45	599	1580	0.38	0.051155	0.002560	0.174320	0.009628	0.024510	0.000386	255.6	119.4	163.2	8.3	156.1	2.4
	JLN-22-11	33	629	1069	0.59	0.053205	0.002855	0.182612	0.009066	0.025104	0.000323	344.5	120.4	170.3	7.8	159.8	2
	JLN-22-12	38	534	1289	0.41	0.049145	0.001838	0.172618	0.007220	0.025275	0.000323	153.8	87.0	161.7	6.3	160.9	2
	JLN-22-13	43	547	1530	0.36	0.050774	0.001659	0.176809	0.005601	0.025438	0.000365	231.6	75.9	165.3	4.8	161.9	2.3
	JLN-22-15	39	425	1359	0.31	0.053104	0.001791	0.190402	0.006989	0.025883	0.000323	331.5	77.8	177.0	6.0	164.7	2
	JLN-22-17	12	224	406	0.55	0.054626	0.003927	0.189196	0.013262	0.025308	0.000387	398.2	161.1	175.9	11.3	161.1	2.4
	JLN-22-20	9	179	294	0.61	0.050734	0.003935	0.172818	0.012790	0.025701	0.000673	227.8	179.6	161.9	11.1	163.6	4.2
	JLN-22-22	16	253	513	0.49	0.053286	0.004386	0.182819	0.013357	0.025543	0.000425	342.7	187.0	170.5	11.5	162.6	2.7
	JLN-22-23	23	330	771	0.43	0.047877	0.003038	0.163798	0.009770	0.025215	0.000362	100.1	135.2	154.0	8.5	160.5	2.3
	JLN-22-27	47	589	1615	0.36	0.050121	0.002021	0.177826	0.007777	0.025661	0.000364	211.2	97.2	166.2	6.7	163.3	2.3
Phase II	DYL801-36-2-1	64	929	2204	0.42	0.051660	0.000998	0.180765	0.004007	0.025368	0.000364	333.4	44.4	168.7	3.4	161.5	2.3
	DYL801-36-2-2	8	197	275	0.72	0.050808	0.003136	0.170759	0.009956	0.024905	0.000415	231.6	142.6	160.1	8.6	158.6	2.6
	DYL801-36-2-4	6	111	208	0.53	0.054841	0.002846	0.183358	0.009644	0.024497	0.000347	405.6	116.7	170.9	8.3	156.0	2.2
	DYL801-36-2-6	42	477	1531	0.31	0.050124	0.000876	0.175001	0.002914	0.025367	0.000180	211.2	38.0	163.8	2.5	161.5	1.1
	DYL801-36-2-7	18	426	614	0.69	0.049269	0.001505	0.169303	0.004912	0.025012	0.000254	161.2	72.2	158.8	4.3	159.3	1.6
	DYL801-36-2-8	14	233	515	0.45	0.049367	0.001913	0.167457	0.006301	0.024707	0.000335	164.9	90.7	157.2	5.5	157.3	2.1
	DYL801-36-2-9	13	374	387	0.97	0.054743	0.002265	0.187703	0.007472	0.025021	0.000252	466.7	97.2	174.7	6.4	159.3	1.6
	DYL801-36-2-10	9	107	336	0.32	0.052979	0.003202	0.181470	0.010735	0.025022	0.000352	327.8	138.9	169.3	9.2	159.3	2.2
	DYL801-36-2-12	28	335	1031	0.33	0.049642	0.001304	0.171026	0.004745	0.024920	0.000199	189.0	58.3	160.3	4.1	158.7	1.3
	DYL801-36-2-13	18	306	592	0.52	0.049909	0.001640	0.174271	0.005697	0.025324	0.000231	190.8	71.3	163.1	4.9	161.2	1.5
	DYL801-36-2-14	29	379	1042	0.36	0.053046	0.001412	0.182105	0.004869	0.024952	0.000235	331.5	28.7	169.9	4.2	158.9	1.5
	DYL801-36-2-15	16	368	538	0.68	0.054120	0.001838	0.185078	0.006097	0.024885	0.000277	376.0	75.9	172.4	5.2	158.5	1.7
	DYL801-36-2-16	14	191	505	0.38	0.047778	0.001663	0.161389	0.005448	0.024933	0.000614	87.1	−115.7	151.9	4.8	158.8	3.9
	DYL801-36-2-18	11	205	367	0.56	0.046117	0.001928	0.155906	0.006498	0.024605	0.000244	400.1	−298.1	147.1	5.7	156.7	1.5
	DYL801-36-2-22	14	185	472	0.39	0.053567	0.002911	0.182347	0.009691	0.024807	0.000466	353.8	119.4	170.1	8.3	158.0	2.9
	DYL801-36-2-23	14	269	462	0.58	0.053019	0.001685	0.179385	0.005555	0.024648	0.000300	327.8	104.6	167.5	4.8	157.0	1.9
	DYL801-36-2-24	39	145	706	0.21	0.056172	0.001149	0.383593	0.009000	0.049373	0.000597	457.5	46.3	329.7	6.6	310.7	3.7
	DYL801-36-2-26	20	200	704	0.28	0.053615	0.003049	0.183274	0.009243	0.025244	0.000546	353.8	129.6	170.9	7.9	160.7	3.4
	DYL801-36-2-27	13	359	425	0.84	0.052543	0.002532	0.178024	0.007970	0.024808	0.000247	309.3	111.1	166.4	6.9	158.0	1.6
	DYL801-36-2-28	29	461	1025	0.45	0.049717	0.001361	0.167672	0.004404	0.024489	0.000215	189.0	63.0	157.4	3.8	156.0	1.4
	DYL801-36-2-29	9	156	304	0.51	0.052432	0.002407	0.177278	0.007687	0.024808	0.000323	305.6	105.5	165.7	6.6	158.0	2
	DYL801-36-2-30	18	229	676	0.34	0.049702	0.001993	0.167666	0.006554	0.024574	0.000271	189.0	94.4	157.4	5.7	156.5	1.7
Phase III	JLN-11-1	20	347	656	0.53	0.051949	0.001258	0.177413	0.004025	0.024798	0.000431	283.4	55.6	165.8	3.5	157.9	2.7
	JLN-11-2	21	454	661	0.69	0.057430	0.004521	0.191182	0.018144	0.023879	0.000465	509.3	174.1	177.6	15.5	152.1	2.9
	JLN-11-3	11	262	363	0.72	0.055444	0.001350	0.186753	0.005396	0.024449	0.000590	431.5	53.7	173.9	4.6	155.7	3.7
	JLN-11-4	31	1011	902	1.12	0.051786	0.001429	0.174912	0.003325	0.024692	0.000480	276.0	63.0	163.7	2.9	157.2	3
	JLN-11-6	36	1147	1075	1.07	0.049150	0.001126	0.167993	0.005956	0.024780	0.000789	153.8	53.7	157.7	5.2	157.8	5.0
	JLN-11-7	19	595	576	1.03	0.054256	0.002171	0.183320	0.007521	0.024477	0.000463	388.9	88.9	170.9	6.5	155.9	2.9
	JLN-11-12	29	746	920	0.81	0.054332	0.001414	0.183794	0.005104	0.024503	0.000437	383.4	59.3	171.3	4.4	156.1	2.7
	JLN-11-13	15	288	485	0.59	0.048554	0.000992	0.167272	0.005219	0.024933	0.000625	127.9	48.1	157.0	4.5	158.8	3.9
	JLN-11-14	46	960	1525	0.63	0.053461	0.002072	0.179827	0.006563	0.024382	0.001083	350.1	88.9	167.9	5.6	155.3	6.8
	JLN-11-17	19	703	547	1.28	0.051230	0.002529	0.168615	0.008721	0.023866	0.001460	250.1	80.5	158.2	7.6	152.0	9.2
	JLN-11-18	47	766	1601	0.48	0.053629	0.001711	0.184745	0.010364	0.024798	0.000970	353.8	75.0	172.1	8.9	157.9	6.1
	JLN-11-21	20	397	646	0.61	0.053537	0.001445	0.182057	0.005697	0.024497	0.000474	350.1	56.5	169.8	4.9	156.0	3.0
	JLN-11-23	49	610	1742	0.35	0.052408	0.000948	0.179404	0.004175	0.024679	0.000481	301.9	40.7	167.5	3.6	157.2	3.0

(*continued on next page*)

Table 2 (*continued*)

	Spots	Concentrations (ppm)			Th/U	Isotopic ratios						Isotopic Ages (Ma)					
		Pb	Th	U		$^{207}Pb/^{206}Pb$	± σ	$^{207}Pb/^{235}U$	± σ	$^{206}Pb/^{238}U$	± σ	$^{207}Pb/^{206}Pb$	± σ	$^{207}Pb/^{235}U$	± σ	$^{206}Pb/^{238}U$	± σ
	JLN-11-25	40	1295	1190	1.09	0.052678	0.002375	0.184049	0.012611	0.025107	0.000770	322.3	101.8	171.5	10.8	159.8	4.8
	JLN-11-30	20	312	696	0.45	0.053144	0.001548	0.182584	0.006023	0.024805	0.000611	344.5	32.4	170.3	5.2	158.0	3.8
	JLN-11-33	49	683	1717	0.40	0.052406	0.001026	0.180747	0.004389	0.024933	0.000486	301.9	44.4	168.7	3.8	158.8	3.1
	JLN-11-34	14	352	437	0.81	0.053351	0.002244	0.182033	0.005606	0.024936	0.000655	342.7	89.8	169.8	4.8	158.8	4.1
	JLN-11-35	23	236	803	0.29	0.052146	0.001330	0.179577	0.003789	0.025025	0.000493	300.1	59.3	167.7	3.3	159.3	3.1
	JLN-11-36	56	401	2055	0.19	0.053348	0.000803	0.182033	0.004000	0.024658	0.000393	342.7	33.3	169.8	3.4	157.0	2.5
	JLN-11-37	23	785	671	1.17	0.054524	0.004414	0.188118	0.010995	0.025055	0.000731	394.5	176.8	175.0	9.4	159.5	4.6
Phase IV	JLN-15-2	6	97	196	0.50	0.050554	0.009775	0.176191	0.039791	0.024219	0.001285	220.4	396.2	164.8	34.4	154.3	8.1
	JLN-15-3	10	206	342	0.60	0.052038	0.004715	0.172314	0.014697	0.024035	0.000641	287.1	209.2	161.4	12.7	153.1	4.0
	JLN-15-4	4	159	131	1.22	0.053237	0.009719	0.181372	0.023807	0.024886	0.001311	338.9	366.6	169.2	20.5	158.5	8.2
	JLN-15-5	8	190	259	0.74	0.052281	0.006258	0.173454	0.022548	0.024146	0.000732	298.2	251.8	162.4	19.5	153.8	4.6
	JLN-15-6	124	1731	4489	0.39	0.050184	0.001266	0.167810	0.004410	0.024244	0.000337	211.2	59.2	157.5	3.8	154.4	2.1
	JLN-15-8	25	756	692	1.09	0.053301	0.007155	0.183663	0.025820	0.024841	0.000874	342.7	110.2	171.2	22.2	158.2	5.5
	JLN-15-9	12	208	400	0.52	0.049814	0.002831	0.166948	0.009104	0.024661	0.000382	187.1	133.3	156.8	7.9	157.0	2.4
	JLN-15-10	19	288	227	1.26	0.051643	0.002794	0.440440	0.024767	0.061391	0.001183	333.4	125.9	370.6	17.5	384.1	7.2
	JLN-15-11	19	271	299	0.90	0.054358	0.002965	0.365714	0.019603	0.049151	0.000721	387.1	124.1	316.5	14.6	309.3	4.4
	JLN-15-12	8	248	258	0.96	0.054348	0.004266	0.185722	0.014522	0.024804	0.000586	387.1	177.8	173.0	12.4	157.9	3.7
	JLN-15-13	48	1110	1551	0.72	0.053493	0.002956	0.182105	0.010550	0.024590	0.000489	350.1	128.7	169.9	9.1	156.6	3.1
	JLN-15-14	11	195	392	0.50	0.051576	0.003085	0.169150	0.010410	0.023871	0.000384	264.9	137.0	158.7	9.0	152.1	2.4
	JLN-15-16	12	349	403	0.87	0.052619	0.004084	0.168811	0.011871	0.023987	0.000515	322.3	177.8	158.4	10.3	152.8	3.2
	JLN-15-17	31	960	971	0.99	0.047715	0.002058	0.158882	0.006685	0.024318	0.000327	83.4	100.0	149.7	5.9	154.9	2.1
	JLN-15-19	22	729	707	1.03	0.052329	0.002744	0.171899	0.009166	0.023941	0.000338	298.2	120.4	161.1	7.9	152.5	2.1
	JLN-15-20	45	517	1617	0.32	0.048827	0.001509	0.165717	0.005186	0.024704	0.000254	139.0	72.2	155.7	4.5	157.3	1.6
	JLN-15-21	27	387	939	0.41	0.054037	0.003789	0.179991	0.012486	0.024211	0.000463	372.3	159.2	168.1	10.7	154.2	2.9
	JLN-15-22	6	263	169	1.56	0.053106	0.006963	0.175631	0.022472	0.023852	0.001268	331.5	102.8	164.3	19.4	152.0	8.0
	JLN-15-23	38	288	411	0.70	0.062266	0.003425	0.626316	0.033632	0.073300	0.001207	683.3	118.5	493.8	21.0	456.0	7.2
	JLN-15-24	19	403	404	1.00	0.055763	0.005762	0.289250	0.032523	0.036994	0.000871	442.6	231.4	258.0	25.6	234.2	5.4
	JLN-15-26	53	366	1999	0.18	0.053374	0.002031	0.177303	0.006706	0.024201	0.000355	346.4	85.2	165.7	5.8	154.2	2.2
	JLN-15-28	98	3327	3396	0.98	0.053597	0.001448	0.174268	0.004583	0.023568	0.000198	353.8	56.5	163.1	4.0	150.2	1.2
	JLN-15-29	10	232	323	0.72	0.053060	0.003495	0.170624	0.010271	0.024375	0.000443	331.5	150.0	160.0	8.9	155.2	2.8
	JLN-15-31	10	216	357	0.61	0.051796	0.003260	0.174380	0.011005	0.024435	0.000395	276.0	144.4	163.2	9.5	155.6	2.5
	JLN-15-32	32	1303	969	1.35	0.054490	0.003647	0.176486	0.011184	0.023718	0.000336	390.8	182.4	165.0	9.7	151.1	2.1
	JLN-15-33	23	156	563	0.28	0.055232	0.002553	0.279517	0.013101	0.036549	0.000391	420.4	99.1	250.3	10.4	231.4	2.4
	JLN-15-37	55	1022	1933	0.53	0.052018	0.002390	0.176273	0.008751	0.024433	0.000342	287.1	105.5	164.8	7.6	155.6	2.2
	JLN-15-38	180	3023	6291	0.48	0.053024	0.002590	0.180096	0.011072	0.024536	0.000712	331.5	109.2	168.1	9.5	156.3	4.5
	JLN-15-40	27	814	774	1.05	0.050972	0.006607	0.178249	0.021216	0.025805	0.000758	239.0	283.3	166.6	18.3	164.2	4.8

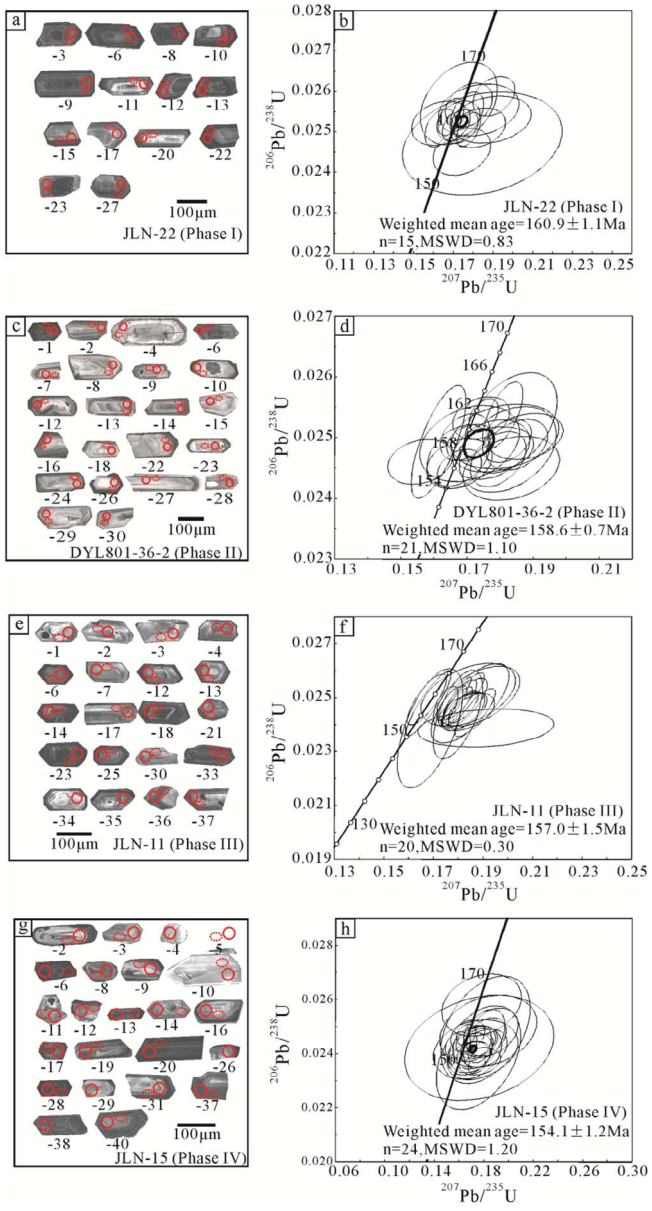

Fig. 4. Cathodoluminescence images and concordia diagrams of zircon U-Pb data for representative granites of the Jiulongnao complex. (a)-(b) Phase I (JLN-22); (c)-(d) Phase II (DYL801-36-2); (e)-(f) Phase III (JLN-11); (g)-(h) Phase IV (JLN-15). Circles denote the LA-ICP-MS analyses for U-Pb dating, and ellipses indicate the LA-ICP-MS Lu-Hf analysis spots.

3. Analytical methods

3.1. LA-ICP-MS zircon U-Pb-Hf analysis

Zircons for U-Pb analysis were separated by conventional magnetic and density techniques and then handpicked under a binocular microscope. The grains were mounted in an epoxy disc and polished to approximate half their thickness. The grains were examined under transmitted and reflected light, and cathodoluminescence (CL) images were used to select spots for U-Pb isotope analyses.

Zircon U-Pb dating was conducted by laser ablation inductively coupled plasma mass spectrometry (LA-ICP-MS) at the MLR Key Laboratory of Metallogeny and Mineral Assessment, Institute of Mineral Resources (IMR), Chinese Academy of Geological Sciences (CAGS), Beijing, using a Thermo Neptune MC-ICP-MS and the associated Newwave UP213 laser ablation system. The analytical spots are 30 μm in diameter. Each analysis incorporated a background acquisition of approximately 15 s (gas blank) followed by 45 s data acquisition from the sample. See Hou et al. (2009) for details of the analytical procedures. Data processing was conducted with the ICPMSDataCal program (Liu et al., 2010), and the zircon concordia age diagrams were obtained using the Isoplot 3.0 program of Ludwig (2003). The tested accuracy of $^{207}Pb/^{206}Pb$, $^{206}Pb/^{238}U$ and $^{207}Pb/^{235}U$ from uniform zircon grains (2σ) is about 2% and the standard zircon dating precision and accuracy is at 1% (2σ). The standard zircon Plesovice was dated as an unknown and yielded a weighted mean $^{206}Pb/^{238}U$ age of 337.13 ± 0.37 Ma (Sláma et al., 2008).

Zircon Hf isotope analyses were carried out in-situ using a NewWave UP213 laser-ablation microprobe, attached to a Thermo Neptune multi-collector ICP-MS at the National Research Center for Geoanalysis (NRCG), CAGS. Instrumental conditions and data acquisition techniques have been comprehensively described by Hou et al. (2007). Lu-Hf isotopic measurements were carried out on the same zircon grains previously analyzed for U-Pb isotopes, with ablation pits of 20 μm in diameter, a repetition rate of 4 Hz, and an ablation time of 32 s. Zircon Plešovice was used as the reference standard during the analyses, and yielded a weighted mean $^{176}Hf/^{177}Hf$ ratio of 0.282480 ± 30 (2σ), agreeing well with the published value (0.282482 ± 13) (Sláma et al., 2008).

3.2. Whole-rock major and trace element and Sr-Nd isotope analyses

Whole-rock major and trace element compositions were determined at NRCG, CAGS. Major element analyses were determined by X-ray fluorescence spectrometry (XRF) using fused glass discs, with precisions of 1–2%. Trace element analyses were determined by inductively coupled plasma-mass spectrometry (ICP-MS) (PE-300D). Precision for most trace elements was generally better than 5% RSD (relative standard deviation), and the measured values Zr, Hf, Nb and Ta are within 10% of the certified values. The detailed sample preparation, instrument operating conditions, and calibration procedures followed those established by Qi et al. (2000).

Sr and Nd isotopic ratios were measured using the MAT262 mass spectrometer and Nu Plasma HR MC-ICP-MS, respectively, at the Key Laboratory of Isotope Geology, Institute of Geology (IG), CAGS following the procedure of He et al. (2007). The measured $^{87}Sr/^{86}Sr$ and $^{143}Nd/^{144}Nd$ ratios were corrected for mass fractionation using $^{88}Sr/^{86}Sr = 8.37521$, and $^{146}Nd/^{144}Nd = 0.7219$, respectively. During the period of data collection, the measured values for SRM 987 $SrCO_3$ and GSB 04-3258-2015 standards were $^{87}Sr/^{86}Sr = 0.710231 \pm 12$ (2σ), and $^{143}Nd/^{144}Nd = 0.512439 \pm 10$ (2σ), respectively.

3.3. In-situ EPMA and fs-LA-ICP-MS analyses of minerals

Major element compositions of minerals were determined with a JEOL-JXA-8230 electron microprobe at the IMR, CAGS. Prior to analysis, thin sections were carbon coated to create a conductive surface. The electron microprobe was operated with an accelerating voltage of 15 kV, a current of 20nA, and an electron beam with a diameter of 5 or 1 μm, according to mineral grain size. Natural minerals and synthetic glasses were used as standards. ZAF corrections were applied to the raw data.

Trace elements of minerals were measured at NRCG, CAGS. Laser sampling was carried out by fs-LA-ICP-MS, using a femto-second laser ablation system (ASI J200) coupled to an inductively-coupled mass spectrometer (Thermo X series II). Helium was used as the carrier gas,

Table 3
LA-ICP-MS zircon Lu-Hf data for granites of the Jiulongnao complex.

	Spot	t(Ma)	$^{176}Yb/^{177}Hf$	$^{176}Lu/^{177}Hf$	$^{176}Hf/^{177}Hf$	2σ	$e^{\lambda t}$	$(^{176}Hf/^{177}Hf)_i$	$\varepsilon_{Hf}(0)$	$\varepsilon_{Hf}(t)$	$f_{Lu/Hf}$	T_{2DM}(Ga)
Phase I	JLN-22-3	159.8	0.039877	0.001412	0.282340	0.000016	1.002987921	0.282336	−15.3	−11.9	−0.96	2.0
	JLN-22-4	157.4	0.033664	0.001153	0.282312	0.000018	1.00294298	0.282309	−16.3	−12.9	−0.97	2.0
	JLN-22-6	161.5	0.060327	0.002120	0.282350	0.000015	1.003019755	0.282344	−14.9	−11.6	−0.94	1.9
	JLN-22-9	160.0	0.044659	0.001534	0.282334	0.000017	1.002991666	0.282329	−15.5	−12.2	−0.95	2.0
	JLN-22-10	156.1	0.118787	0.004004	0.282338	0.000019	1.002918638	0.282326	−15.4	−12.3	−0.88	2.0
	JLN-22-11	159.8	0.035697	0.001243	0.282313	0.000018	1.002988592	0.282309	−16.2	−12.9	−0.96	2.0
	JLN-22-12	160.9	0.032818	0.001135	0.282308	0.000016	1.003008621	0.282305	−16.4	−13.0	−0.97	2.0
	JLN-22-13	161.9	0.052215	0.001839	0.282390	0.000018	1.003027919	0.282385	−13.5	−10.1	−0.94	1.8
	JLN-22-15	164.7	0.037786	0.001331	0.282358	0.000019	1.003080289	0.282354	−14.6	−11.2	−0.96	1.9
	JLN-22-17	161.1	0.026275	0.000918	0.282356	0.000018	1.003012502	0.282353	−14.7	−11.3	−0.97	1.9
	JLN-22-20	163.6	0.061370	0.002179	0.282284	0.000017	1.003059081	0.282278	−17.2	−13.9	−0.93	2.1
	JLN-22-22	162.6	0.055967	0.001923	0.282310	0.000018	1.003040262	0.282305	−16.3	−13.0	−0.94	2.0
	JLN-22-23	160.5	0.023393	0.000807	0.282366	0.000015	1.003001623	0.282364	−14.3	−10.9	−0.98	1.9
	JLN-22-27	163.3	0.057875	0.001959	0.282333	0.000018	1.003054078	0.282327	−15.5	−12.1	−0.94	2.0
Phase II	DYL801-36-2-1	161.5	0.041899	0.001411	0.282318	0.000013	1.003019755	0.282314	−16.1	−12.7	−0.96	2.0
	DYL801-36-2-2	158.6	0.033692	0.001110	0.282300	0.000015	1.00296545	0.282297	−16.7	−13.3	−0.97	2.0
	DYL801-36-2-4	156.0	0.021344	0.000754	0.282316	0.000017	1.002916766	0.282314	−16.1	−12.8	−0.98	2.0
	DYL801-36-2-6	161.5	0.039291	0.001347	0.282333	0.000015	1.003019755	0.282329	−15.5	−12.1	−0.96	2.0
	DYL801-36-2-7	159.3	0.045989	0.001501	0.282346	0.000018	1.002978558	0.282342	−15.1	−11.7	−0.95	1.9
	DYL801-36-2-8	157.3	0.021464	0.000723	0.282355	0.000017	1.002941108	0.282353	−14.7	−11.4	−0.98	1.9
	DYL801-36-2-9	159.3	0.033888	0.001162	0.282281	0.000017	1.002978558	0.282277	−17.4	−14.0	−0.96	2.1
	DYL801-36-2-10	159.3	0.021758	0.000724	0.282353	0.000016	1.002978558	0.282351	−14.8	−11.4	−0.98	1.9
	DYL801-36-2-12	158.7	0.030789	0.001050	0.282350	0.000017	1.002967323	0.282347	−14.9	−11.5	−0.97	1.9
	DYL801-36-2-13	161.2	0.046858	0.001480	0.282346	0.000018	1.003014137	0.282341	−15.1	−11.7	−0.96	1.9
	DYL801-36-2-14	158.9	0.036190	0.001181	0.282358	0.000016	1.002971068	0.282354	−14.7	−11.3	−0.96	1.9
	DYL801-36-2-15	158.5	0.029368	0.000971	0.282335	0.000016	1.002963578	0.282332	−15.5	−12.1	−0.97	2.0
	DYL801-36-2-16	158.8	0.030217	0.000999	0.282351	0.000018	1.002969195	0.282348	−14.9	−11.5	−0.97	1.9
	DYL801-36-2-18	156.7	0.032218	0.001041	0.282378	0.000016	1.002929873	0.282375	−13.9	−10.6	−0.97	1.9
	DYL801-36-2-22	158.0	0.023703	0.000803	0.282370	0.000016	1.002954215	0.282368	−14.2	−10.8	−0.98	1.9
	DYL801-36-2-23	157.0	0.046766	0.001541	0.282307	0.000017	1.00293549	0.282302	−16.5	−13.2	−0.95	2.0
	DYL801-36-2-26	160.7	0.033340	0.001130	0.282331	0.000018	1.003004774	0.282327	−15.6	−12.2	−0.97	2.0
	DYL801-36-2-27	158.0	0.044937	0.001393	0.282229	0.000016	1.002954215	0.282225	−19.2	−15.9	−0.96	2.2
	DYL801-36-2-28	156.0	0.030671	0.001019	0.282340	0.000017	1.002916766	0.282337	−15.3	−12.0	−0.97	2.0
	DYL801-36-2-29	158.0	0.038064	0.001230	0.282374	0.000017	1.002954215	0.282370	−14.1	−10.7	−0.96	1.9
	DYL801-36-2-30	156.5	0.026422	0.000833	0.282314	0.000017	1.002926128	0.282311	−16.2	−12.9	−0.97	2.0
	DYL801-36-2-24	310.7	0.026785	0.000904	0.282378	0.000016	1.005817626	0.282373	−13.9	−7.3	−0.97	1.8
Phase III	JLN-11-1	157.9	0.020178	0.000724	0.282293	0.000017	1.002952512	0.282291	−16.9	−13.6	−0.98	2.1
	JLN-11-2	152.1	0.024446	0.000856	0.282319	0.000020	1.002844263	0.282316	−16.0	−12.8	−0.97	2.0
	JLN-11-3	155.7	0.042841	0.001373	0.282391	0.000019	1.002911331	0.282387	−13.5	−10.2	−0.96	1.8
	JLN-11-4	157.2	0.082629	0.002640	0.282420	0.000021	1.002940028	0.282412	−12.5	−9.3	−0.92	1.8
	JLN-11-6	157.8	0.052475	0.001684	0.282435	0.000019	1.002950368	0.282431	−11.9	−8.6	−0.95	1.7
	JLN-11-7	155.9	0.034132	0.001144	0.282422	0.000021	1.002914666	0.282419	−12.4	−9.1	−0.97	1.8
	JLN-11-12	156.1	0.045102	0.001535	0.282426	0.000024	1.002917716	0.282422	−12.2	−9.0	-0.95	1.8
	JLN-11-13	158.8	0.025180	0.000913	0.282341	0.000017	1.002968424	0.282338	−15.2	−11.9	−0.97	2.0
	JLN-11-14	155.3	0.041192	0.001416	0.282294	0.000017	1.002903457	0.282290	−16.9	−13.6	−0.96	2.1
	JLN-11-17	152.0	0.058130	0.001962	0.282417	0.000021	1.002842718	0.282411	−12.6	−9.4	−0.94	1.8
	JLN-11-18	157.9	0.029848	0.001053	0.282358	0.000019	1.002952485	0.282355	−14.6	−11.3	−0.97	1.9
	JLN-11-21	156.0	0.042037	0.001427	0.282173	0.000024	1.002916766	0.282169	−21.2	−17.9	−0.96	2.3
	JLN-11-23	157.2	0.030389	0.001079	0.282330	0.000018	1.002939235	0.282327	−15.6	−12.3	−0.97	2.0
	JLN-11-25	159.8	0.046898	0.001575	0.282445	0.000025	1.002987921	0.282440	−11.6	−8.2	−0.95	1.7
	JLN-11-30	158.0	0.038369	0.001275	0.282316	0.000020	1.002954215	0.282313	−16.1	−12.8	−0.96	2.0
	JLN-11-33	158.8	0.017601	0.000545	0.282323	0.000015	1.002969195	0.282321	−15.9	−12.5	−0.98	2.0
	JLN-11-36	157.0	0.020752	0.000746	0.282344	0.000014	1.00293549	0.282342	−15.1	−11.8	−0.98	1.9
	JLN-11-37	159.5	0.055972	0.001908	0.282408	0.000019	1.002982303	0.282402	−12.9	−9.6	−0.94	1.8
Phase IV	JLN-15-2	154.3	0.035277	0.001178	0.282302	0.000020	1.002884934	0.282299	−16.6	−13.3	−0.96	2.0
	JLN-15-3	153.1	0.031315	0.001043	0.282357	0.000017	1.002862466	0.282354	−14.7	−11.4	−0.97	1.9
	JLN-15-5	153.8	0.091835	0.003199	0.282330	0.000015	1.002875573	0.282321	−15.6	−12.6	−0.90	2.0
	JLN-15-6	154.4	0.068784	0.002410	0.282293	0.000022	1.002886807	0.282286	−16.9	−13.8	−0.93	2.1
	JLN-15-8	158.2	0.036098	0.001209	0.282418	0.000018	1.00295796	0.282414	−12.5	−9.2	−0.96	1.8
	JLN-15-9	157.0	0.023123	0.000789	0.282320	0.000017	1.00293549	0.282317	−16.0	−12.6	−0.98	2.0
	JLN-15-12	157.9	0.079431	0.002517	0.282373	0.000023	1.002952343	0.282365	−14.1	−10.9	−0.92	1.9
	JLN-15-13	156.6	0.035133	0.001142	0.282286	0.000017	1.002928	0.282283	−17.2	−13.9	−0.97	2.1
	JLN-15-14	152.1	0.021059	0.000736	0.282325	0.000015	1.002843743	0.282323	−15.8	−12.6	−0.98	2.0
	JLN-15-16	152.8	0.047325	0.001631	0.282344	0.000017	1.002856849	0.282339	−15.1	−12.0	−0.95	2.0
	JLN-15-17	154.9	0.053090	0.001786	0.282421	0.000018	1.002896169	0.282416	−12.4	−9.2	−0.95	1.8
	JLN-15-19	152.5	0.041393	0.001404	0.282378	0.000021	1.002851232	0.282374	−13.9	−10.7	−0.96	1.9
	JLN-15-20	157.3	0.046996	0.001522	0.282381	0.000015	1.002941108	0.282377	−13.8	−10.5	−0.95	1.9
	JLN-15-28	150.2	0.067596	0.002211	0.282357	0.000017	1.00280817	0.282351	−14.7	−11.6	−0.93	1.9
	JLN-15-31	155.6	0.048215	0.001636	0.282345	0.000018	1.002909276	0.282340	−15.1	−11.9	−0.95	2.0
	JLN-15-37	155.6	0.105065	0.003446	0.282346	0.000020	1.002909276	0.282336	−15.1	−12.0	−0.90	2.0
	JLN-15-40	164.2	0.056654	0.002027	0.282353	0.000011	1.003070318	0.282347	−14.8	−11.4	−0.94	1.9
	JLN-15-33	231.4	0.029060	0.000817	0.282260	0.000025	1.004329584	0.282257	−18.1	−13.1	−0.98	2.1
	JLN-15-10	374.1	0.048122	0.001582	0.282740	0.000021	1.007008895	0.282729	−1.1	6.7	−0.95	0.9
	JLN-15-11	309.3	0.020450	0.000860	0.283021	0.000018	1.005791336	0.283016	8.8	15.4	-0.97	0.3

Table 4
Major and trace element data for granites of the Jiulongnao complex.

Sample	JLN-22	JLN-23	JLN-24	JLN-25	DYL601-180-1	DYL601-180-2	DYL801-36-1	DYL801-36-2	DYL801-160-1	DYL801-160-2	JLN-1	JLN-2	JLN-12	JLN-13	JLN-14	JLN-6	JLN-7	JLN-8	JLN-16	JLN-17	JLN-18
Rock type	Phase I				Phase II						Phase III					Phase IV					
Major elements(wt%)																					
SiO_2	77.11	76.11	77.76	77.08	74.56	76.69	75.93	76.77	74.95	76.73	74.43	74.13	74.21	74.42	75.06	77.46	77.27	79.13	76.90	78.87	76.71
TiO_2	0.11	0.10	0.10	0.09	0.08	0.07	0.07	0.08	0.06	0.06	0.20	0.18	0.18	0.18	0.18	0.02	0.02	0.02	0.02	0.02	0.02
Al_2O_3	12.29	12.86	12.07	12.46	12.13	12.24	12.11	12.36	12.87	12.08	13.60	13.63	13.73	13.62	13.34	12.69	12.84	11.79	13.03	11.83	13.04
Fe_2O_3	1.29	1.08	0.46	1.00	0.58	1.13	0.93	1.24	0.64	0.98	1.60	1.48	1.01	1.42	1.48	0.49	0.52	0.69	0.46	0.35	0.48
FeO	0.13	0.16	0.70	0.20	0.75	0.25	0.40	0.25	0.61	0.40	0.20	0.16	0.52	0.16	0.13	0.23	0.27	0.13	0.13	0.27	0.20
MnO	0.09	0.08	0.07	0.07	0.11	0.11	0.10	0.11	0.11	0.11	0.04	0.04	0.07	0.08	0.08	0.16	0.11	0.14	0.06	0.06	0.07
MgO	0.19	0.17	0.16	0.17	0.48	0.21	0.15	0.14	0.10	0.11	0.27	0.27	0.23	0.23	0.24	0.05	0.05	0.05	0.05	0.06	0.06
CaO	0.83	0.91	0.89	0.85	1.52	0.97	0.86	0.84	0.91	0.81	0.65	0.63	0.63	0.61	0.43	0.30	0.38	0.28	0.22	0.20	0.24
Na_2O	2.98	3.22	3.04	3.03	2.98	3.20	3.10	3.21	3.26	3.32	2.53	2.47	2.81	2.86	2.90	3.88	4.03	3.70	3.78	3.80	3.79
K_2O	4.42	4.71	4.29	4.80	4.51	4.19	4.68	4.69	4.79	4.37	5.76	5.87	5.54	5.55	5.27	4.42	4.22	3.85	5.01	3.99	4.89
P_2O_5	0.03	0.02	0.02	0.02	0.03	0.02	0.02	0.02	0.02	0.02	0.04	0.03	0.04	0.04	0.02	0.01	0.01	0.00	0.01	0.01	0.01
Total	100.85	100.86	101.06	100.47	100.86	101.06	100.47	101.46	100.65	100.34	101.07	100.59	101.11	100.72	100.97	100.29	100.47	100.47	100.59	100.39	100.49
CO_2	0.43	0.17	0.26	0.09	1.00	0.83	0.67	0.50	0.50	0.17	0.17	0.17	0.17	0.17	0.17	0.09	0.09	0.09	0.17	0.26	0.17
H_2O^+	0.61	0.55	0.41	0.42	0.76	0.44	0.38	0.36	0.48	0.36	0.74	0.70	1.10	0.57	0.78	0.15	0.21	0.18	0.35	0.25	0.28
LOI	0.60	0.51	0.46	0.48	1.23	0.58	0.66	0.58	0.76	0.50	0.81	0.80	0.86	0.79	0.88	0.31	0.39	0.38	0.38	0.41	0.51
F	0.17	0.09	0.09	0.09	0.14	0.13	0.41	0.31	0.59	0.32	0.03	0.03	0.01	0.02	0.01	0.03	0.06	0.04	0.02	0.01	0.02
Trace elements(ppm)																					
Cl	39.0	43.0	42.0	40.0	226	362	499	456	89.0	201	53.0	48.0	34.0	34.0	34.0	33.0	39.0	34.0	31.0	l.d.l.	40.0
Li	139	127	121	128	179	221	151	125	297	146	154	141	69.6	70.9	66.0	129	201	141	67.7	33.9	65.4
Be	10.3	9.12	8.85	9.52	16.4	16.0	17.2	21.3	15.5	64.9	9.31	7.63	6.80	7.16	7.87	8.99	10.7	8.75	12.8	26.7	14.3
Cr	2.33	2.38	2.11	3.87	107	97.9	93.6	97.3	86.7	84.8	1.68	4.73	5.96	2.42	12.0	1.15	1.68	1.44	2.13	1.84	1.39
Mn	680	568	538	579	979	907	863	954	946	897	297	266	472	521	552	1108	744	1010	452	401	511
Co	1.10	0.95	1.00	1.00	2.34	1.50	1.41	1.69	1.14	1.36	1.36	1.38	1.23	1.20	1.25	0.13	0.14	0.15	0.34	0.24	0.39
Ni	1.21	1.08	0.66	0.96	12.1	11.0	9.14	10.7	15.8	10.5	0.98	1.16	1.04	0.89	5.36	0.37	0.87	0.49	1.24	0.65	0.85
Ga	20.3	20.1	18.4	19.9	22.6	23.6	21.7	22.5	23.3	22.2	22.8	21.8	21.6	21.0	21.6	23.4	23.7	22.2	24.0	25.9	25.1
Rb	449	405	384	473	616	575	670	627	744	616	358	365	396	395	412	782	754	704	776	596	762
Sr	36.2	38.7	36.4	39.0	42.2	32.3	33.5	35.4	27.0	26.3	85.6	81.8	99.9	94.2	90.9	1.80	1.99	2.02	8.14	8.92	10.1
Cs	31.3	32.5	31.9	34.9	24.4	26.3	22.4	20.0	24.1	25.7	24.5	21.5	17.2	17.3	19.2	28.1	28.8	29.1	44.6	26.3	43.0
Ba	82.5	84.3	77.6	77.2	54.7	49.1	66.8	58.2	48.1	33.8	479	546	515	475	512	3.96	3.42	4.59	23.7	16.4	25.6
Th	37.8	34.8	39.3	45.4	39.5	47.1	46.7	42.2	40.5	35.1	43.7	38.5	42.8	41.9	43.6	16.6	11.0	14.5	11.5	15.0	15.7
Zr	103	91.3	104	99.6	73.7	176	72.8	83.0	59.9	93.3	166	155	163	160	174	68.9	73.9	67.5	23.4	50.4	38.7
Hf	4.77	4.39	5.10	4.94	4.11	9.19	3.82	4.28	3.56	5.35	5.58	5.33	5.63	5.52	6.35	6.50	6.33	6.02	3.84	10.7	4.66
Ti	690	613	574	608	524	465	500	533	388	368	1101	989	929	968	1034	87.6	102	111	103	90.9	133
W	2.40	1.61	1.27	1.57	6.18	5.90	4.05	2.52	10.3	8.92	0.82	0.78	0.78	0.64	1.34	4.46	5.73	4.55	9.09	9.52	5.17
Sn	36.8	20.1	19.6	20.5	23.7	22.8	25.6	23.7	34.6	26.8	12.5	11.5	11.3	10.5	12.8	17.7	22.4	20.1	15.8	11.0	15.1
Mo	0.13	0.12	0.14	0.12	0.87	0.98	0.84	0.90	0.84	0.83	0.15	0.17	0.14	0.11	0.29	0.05	0.09	l.d.l.	0.09	0.60	0.15
Bi	3.62	2.47	1.16	2.24	0.65	0.95	0.31	0.36	1.71	0.36	0.49	0.22	0.09	0.12	0.13	0.54	0.53	0.44	11.2	14.2	5.71
Nb	20.2	18.7	24.2	22.0	32.7	44.8	33.7	31.5	44.3	37.7	25.9	23.2	21.4	21.3	25.0	29.2	32.0	30.2	28.3	34.3	28.2
Ta	5.68	5.55	5.50	5.80	22.6	28.4	24.2	21.4	31.8	28.9	3.42	3.13	2.89	3.05	4.01	11.2	12.2	11.5	35.0	60.6	25.8
U	11.5	11.1	13.8	13.2	23.3	31.4	15.7	12.2	23.2	22.9	6.54	5.86	6.93	6.45	8.04	11.4	14.0	10.5	11.8	19.0	11.9
La	18.6	18.8	17.3	25.1	15.7	17.2	19.2	20.0	18.8	14.2	61.9	54.9	58.6	57.3	61.0	2.54	2.03	2.34	6.13	7.77	6.84
Ce	38.9	36.8	35.0	49.8	35.5	38.4	41.1	44.7	40.4	32.9	113	104	113	116	114	6.33	9.88	5.91	13.4	16.8	12.6
Pr	5.06	5.16	4.72	6.39	4.44	4.70	5.17	5.57	4.83	4.23	13.2	11.3	12.1	11.6	12.3	0.68	0.60	0.63	1.71	1.93	1.86
Nd	20.6	20.6	20.1	25.6	17.4	18.1	19.4	21.4	18.0	17.2	46.6	42.7	44.7	40.8	44.5	3.01	2.73	2.82	7.56	7.66	7.88
Sm	5.89	5.78	5.91	6.98	5.99	5.89	6.09	6.70	5.61	6.89	8.26	7.33	7.58	7.38	7.67	1.74	1.54	1.43	3.01	3.14	3.33
Eu	0.30	0.33	0.30	0.32	0.26	0.21	0.24	0.24	0.18	0.18	0.69	0.66	0.68	0.65	0.66	l.d.l.	l.d.l.	l.d.l.	l.d.l.	l.d.l.	0.06
Gd	6.34	6.27	6.47	7.34	8.55	8.12	7.83	8.76	7.00	9.87	6.45	5.55	5.88	5.60	5.10	3.59	3.06	2.80	4.26	3.91	4.99
Tb	1.18	1.14	1.23	1.34	1.65	1.53	1.45	1.54	1.29	1.93	0.88	0.75	0.73	0.74	0.80	0.99	0.81	0.77	1.00	0.99	1.22
Dy	8.06	7.63	8.15	9.03	11.4	11.0	9.77	10.3	8.94	13.1	5.36	4.65	4.07	3.98	4.52	9.74	7.51	7.55	7.66	7.15	9.45
Ho	1.69	1.62	1.78	1.89	2.53	2.43	2.11	2.20	1.94	2.84	0.99	0.90	0.69	0.67	0.84	2.83	1.88	2.12	1.65	1.66	2.18

(*continued on next page*)

Table 4 (*continued*)

Sample	JLN-22	JLN-23	JLN-24	JLN-25	DYL601-180-1	DYL601-180-2	DYL801-36-1	DYL801-36-2	DYL801-160-1	DYL801-160-2	JLN-1	JLN-2	JLN-12	JLN-13	JLN-14	JLN-6	JLN-7	JLN-8	JLN-16	JLN-17	JLN-18
Rock type	Phase I				Phase II						Phase III					Phase IV					
Er	5.44	5.04	5.64	5.99	8.16	7.94	6.70	6.99	6.37	9.11	3.21	2.88	2.19	2.21	2.55	11.8	7.32	9.25	5.53	5.61	7.50
Tm	0.87	0.84	0.87	0.96	1.32	1.31	1.10	1.13	1.02	1.49	0.45	0.41	0.30	0.31	0.37	2.41	1.45	1.85	0.98	1.00	1.38
Yb	6.36	5.69	6.34	6.73	9.21	9.06	7.62	7.76	7.28	10.2	2.98	2.74	2.04	2.16	2.51	20.1	11.8	15.7	7.11	7.71	10.3
Lu	0.93	0.89	0.89	0.98	1.41	1.43	1.17	1.20	1.13	1.55	0.43	0.40	0.29	0.32	0.38	3.29	1.96	2.60	1.01	1.16	1.56
Sc	4.58	4.08	4.06	4.25	7.51	6.30	5.70	5.53	5.78	6.95	3.58	3.43	3.03	3.28	3.38	2.82	3.36	3.78	1.80	3.42	3.95
Y	54.1	52.6	55.3	60.2	79.2	69.6	63.0	65.1	57.0	83.2	30.3	27.4	20.1	21.9	24.9	71.4	47.8	57.9	54.4	54.5	73.0
A/CNK	1.10	1.07	1.07	1.06	0.97	1.06	1.03	1.04	1.05	1.03	1.17	1.18	1.17	1.15	1.18	1.08	1.08	1.09	1.08	1.08	1.09
A/NK	1.27	1.24	1.25	1.22	1.24	1.25	1.19	1.19	1.22	1.18	1.31	1.31	1.29	1.27	1.27	1.14	1.15	1.15	1.12	1.12	1.13
T_{Zr}(°C)	760	746	759	754	720	802	726	737	712	746	804	798	802	799	810	726	731	727	648	704	683
Nb/Ta	3.56	3.37	4.40	3.79	1.44	1.58	1.39	1.47	1.39	1.30	7.57	7.41	7.40	6.98	6.23	2.61	2.62	2.63	0.81	0.57	1.09
Rb/Sr	12.4	10.5	10.5	12.1	14.6	17.8	20.0	17.7	27.6	23.4	4.18	4.46	3.96	4.19	4.53	434	379	349	95.3	66.8	75.4
Zr/Hf	21.6	20.8	20.4	20.2	17.9	19.1	19.1	19.4	16.8	17.4	29.7	29.1	29.0	29.0	27.4	10.6	11.7	11.2	6.09	4.71	8.30
ΣREE	120	117	115	148	124	127	129	138	123	126	264	239	253	250	257	69.1	52.6	55.8	61.0	66.5	71.2
$(La/Yb)_N$	1.99	2.24	1.85	2.53	1.16	1.29	1.71	1.75	1.75	0.95	14.1	13.6	19.5	18.0	16.5	0.09	0.12	0.10	0.59	0.68	0.45
$(La/Sm)_N$	1.97	2.03	1.83	2.25	1.63	1.82	1.97	1.86	2.09	1.29	4.68	4.68	4.83	4.85	4.97	0.91	0.82	1.02	1.27	1.55	1.28
$(Gd/Yb)_N$	0.81	0.89	0.83	0.88	0.75	0.72	0.83	0.91	0.78	0.78	1.75	1.64	2.33	2.10	1.64	0.14	0.21	0.14	0.48	0.41	0.39
δEu	0.15	0.17	0.15	0.14	0.11	0.09	0.11	0.09	0.09	0.07	0.29	0.32	0.31	0.31	0.32	/	/	/	/	/	0.04

l.d.l.: lower than detection limits; LOI: loss on ignition.

A/CNK = $Al_2O_3/(CaO + Na_2O + K_2O)$ (molar ratio); A/NK = $Al_2O_3/(Na_2O + K_2O)$ (molar ratio); $T_{Zr}(°C) = 12{,}900/(2.95 + 0.85 \times M + \ln(49{,}600/Zr_{melt}))$ (Watson and Harrison, 1983), where M = cation ratio (Na + K + 2 × Ca)/(Al × Si) in whole rock.

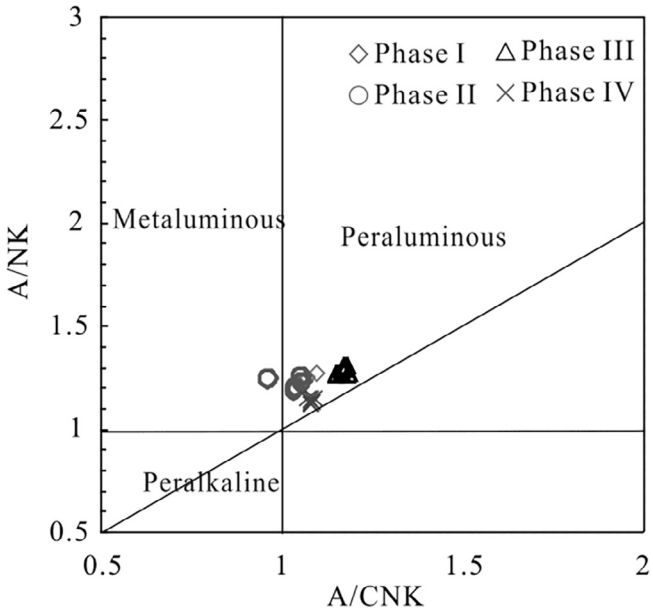

Fig. 5. Plots of A/CNK vs A/NK diagram of rocks from the Jiulongnao complex (after Peccerillo and Taylor, 1976).

with a gas-flow of 0.87 L/min, and argon as the make-up gas; the two were mixed via a T-connector before entering the ICP. The repetition rate was 8 Hz, laser wavelength 343 nm, beam spot size 50 μm (diameter), and the laser power was ~49 mJ/cm^2. Each analysis incorporated a 30 s background acquisition (gas blank) followed by a 50 s data acquisition from the sample. NIST SRM 610 and 612 glasses were used as standard reference materials, and analyzed prior to and after the sample measurements. The NIST SRM 612 was used as an external standard and the average SiO_2 contents of minerals were used as an internal standard. The data were processed using the ICPMSDataCal program (Liu et al., 2008).

4. Analytical results

4.1. Zircon U-Pb dating

Four samples, one each from the four phases of the Jiulongnao complex, were dated using LA-ICP-MS (Table 2).

Zircons from the Jiulongnao complex are euhedral, mostly ~100–200 μm in length, with length-width ratios of 1:1 to 4:1. All of the grains show clear oscillatory zoning (Fig. 4), and have variable Th (58–3227 ppm) and U (131–6676 ppm), with average Th/U ratios of 0.40–0.77. The high Th/U ratios and the oscillatory zoning are indicative of their magmatic origin (Rubatto, 2002).

Zircons from JLN-22 of Phase I, DYL801-36 of Phase II, JLN-11 of Phase III, and JLN-15 of Phase IV yield weighted mean $^{206}Pb/^{238}U$ ages of 160.9 ± 0.6 Ma, 158.6 ± 0.7 Ma, 157.0 ± 1.5 Ma and 154.1 ± 1.2 Ma, respectively (Fig. 4), which can be regarded as the emplacement ages of the four phases.

4.2. Zircon Hf isotopes

In-situ zircon Hf data of the four dated samples are listed in Table 3. Zircons of Phases I-IV have initial $^{176}Hf/^{177}Hf$ ratios of 0.282278–0.282401, 0.282225–0.282375, 0.282169–0.282440 and 0.282283–0.282416, respectively, and $\varepsilon_{Hf}(t)$ values ranging from −13.9 to −9.5, −15.9 to −10.6, −17.9 to −8.2 and −13.9 to −9.1, respectively. Two-stage Hf model ages (T_{2DM}) are 1.8–2.1 Ga, 1.9–2.2 Ga, 1.7–2.3 Ga and 1.8–2.1 Ga, respectively.

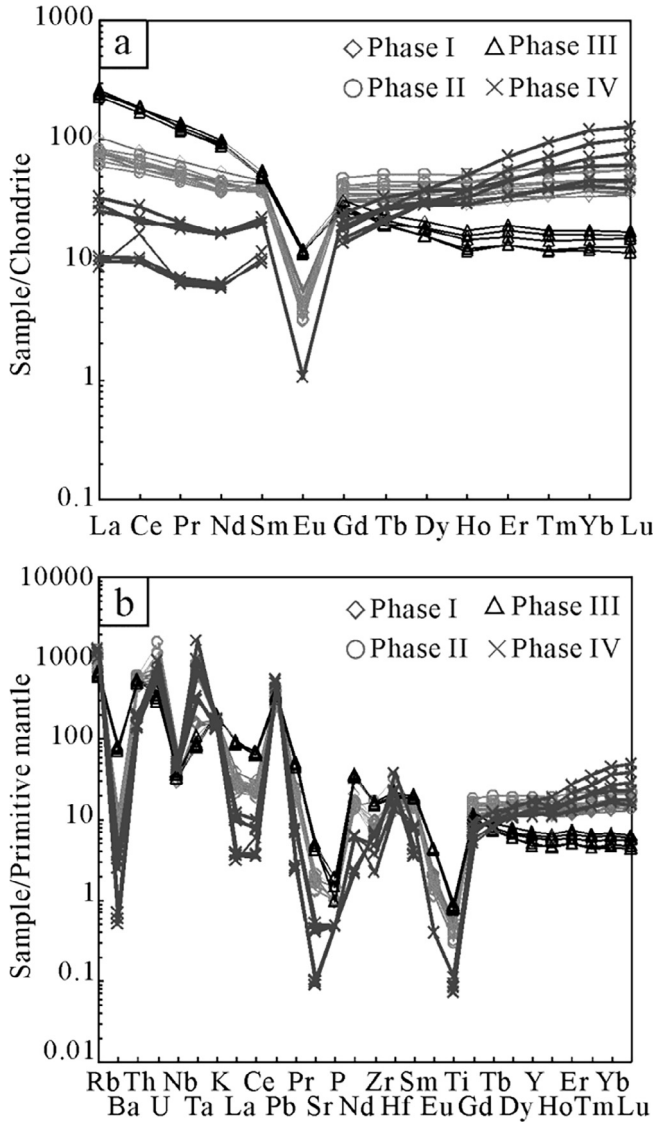

Fig. 6. (a) Chondrite-normalized REE patterns and (b) primitive mantle-normalized trace elements diagrams of rocks from the Jiulongnao complex. The normalization values are from Sun and McDonough (1989).

4.3. Whole-rock major and trace element compositions

Whole-rock major and trace element analytical results of 21 samples from the Jiulongnao complex are listed in Table 4.

All the rocks have high SiO_2 contents ranging from 74.13 wt% to 79.13 wt%. Alkali contents are also high ($Na_2O + K_2O$ = 7.33–8.79 wt %), and K_2O is always higher than Na_2O (K_2O/Na_2O = 1.04–2.38). A plot of A/NK vs. A/CNK (A/NK = molar ratios of $Al_2O_3/(K_2O + Na_2O)$; A/CNK = molar ratios of $Al_2O_3/(CaO + K_2O + Na_2O)$) shows that most samples are peraluminous (Fig. 5).

Rocks of Phases I and II have similar trace element characteristics. Total REE contents are 115–148 ppm and 123–138 ppm; $(La/Yb)_N$ values are 1.85–2.53 and 0.95–1.75; δEu values are 0.14–0.17 and 0.07–0.11, respectively. Chondrite-normalized REE patterns (Fig. 6a) are flat with large negative Eu anomalies. Samples of phase III have high total REE contents ranging from 239 ppm to 264 ppm, with $(La/Yb)_N$ values of 13.6–19.5 and δEu values of 0.29–0.32. The REE patterns of these rocks display LREE enrichment with negative Eu anomalies. Granites of Phase IV have low total REE contents ranging from 53 to 71 ppm, and low $(La/Yb)_N$ and δEu values of 0.09–0.68 and 0.04, respectively. The REE patterns display HREE enrichment with negative Eu anomalies. In the primitive mantle-normalized trace element diagram (Fig. 6b), all the rocks display negative anomalies in Ba, Nb, Sr, P, Eu, Zr and Ti and positive anomalies in Rb, Th, U, Ta and Pb.

The Zr/Hf ratios of rocks from the four phases are 20.2–21.6, 16.8–19.4, 27.4–29.8, and 4.7–11.7, respectively, notably lower than the Zr/Hf ratio of continental crust (36.7) (Rudnick and Gao, 2013). The Nb/Ta ratios are 3.4–4.4, 1.3–1.6, 6.2–7.6, and 0.6–2.6, respectively, significantly lower than the value of the upper crust (13.4) (Rudnick and Gao, 2013).

4.4. Whole-rock Sr-Nd isotopes

Whole-rock Sr-Nd isotopic results are listed in Table 5. Samples JLN-6 and JLN-16 of Phase IV have unrealistically high Rb/Sr and $^{87}Sr/^{86}Sr$ ratios so their initial $^{87}Sr/^{86}Sr$ ratios cannot be used for further discussion (Wu et al., 2002). The other samples have low to moderate initial $^{87}Sr/^{86}Sr$ ratios of 0.7046–0.7157, and $\varepsilon_{Nd}(t)$ values ranging from −10.7 to −9.8.

4.5. Mineral chemistry

4.5.1. Biotite

Biotite occurs as euhedral flakes or irregular grains between

Table 5
Sr-Nd isotopes for granites of the Jiulongnao complex.

	Sample	Rb(ppm)	Sr(ppm)	$^{87}Rb/^{86}Sr$	$^{87}Sr/^{86}Sr$	± 2σ	$(^{87}Sr/^{86}Sr)_i$	Sm(ppm)	Nd(ppm)	$^{147}Sm/^{144}Nd$	$^{143}Nd/^{144}Nd$	± 2σ	$\varepsilon_{Nd}(t)$
Phase I	JLN-22	449	36.2	35.9150	0.790584	14	0.7084	5.89	20.6	0.1740	0.512088	7	−10.3
	JLN-25	473	39.0	35.1184	0.786877	15	0.7065	6.98	25.6	0.1659	0.512090	6	−10.1
Phase II	DYL801-160-1	744	27.0	79.8277	0.886768	14	0.7068	5.61	18.0	0.1895	0.512106	12	−10.2
	DYL601-180-1	616	42.2	42.2825	0.806455	15	0.7111	5.99	17.4	0.2093	0.512150	8	−9.8
	DYL801-36-1	670	33.5	57.8919	0.835122	15	0.7046	6.09	19.4	0.1910	0.512095	10	−10.5
Phase III	JLN-1	358	85.6	12.1101	0.742729	14	0.7157	8.26	46.6	0.1079	0.511999	6	−10.7
	JLN-13	395	94.2	12.1418	0.742364	13	0.7153	7.38	40.8	0.1101	0.512000	6	−10.7
Phase IV	JLN-6	782	1.80	1257.98	\	\	\	1.74	3.01	0.3518	0.512280	14	−10.0
	JL-16	776	8.14	276.04	\	\	\	3.01	7.56	0.2423	0.512193	9	−9.6

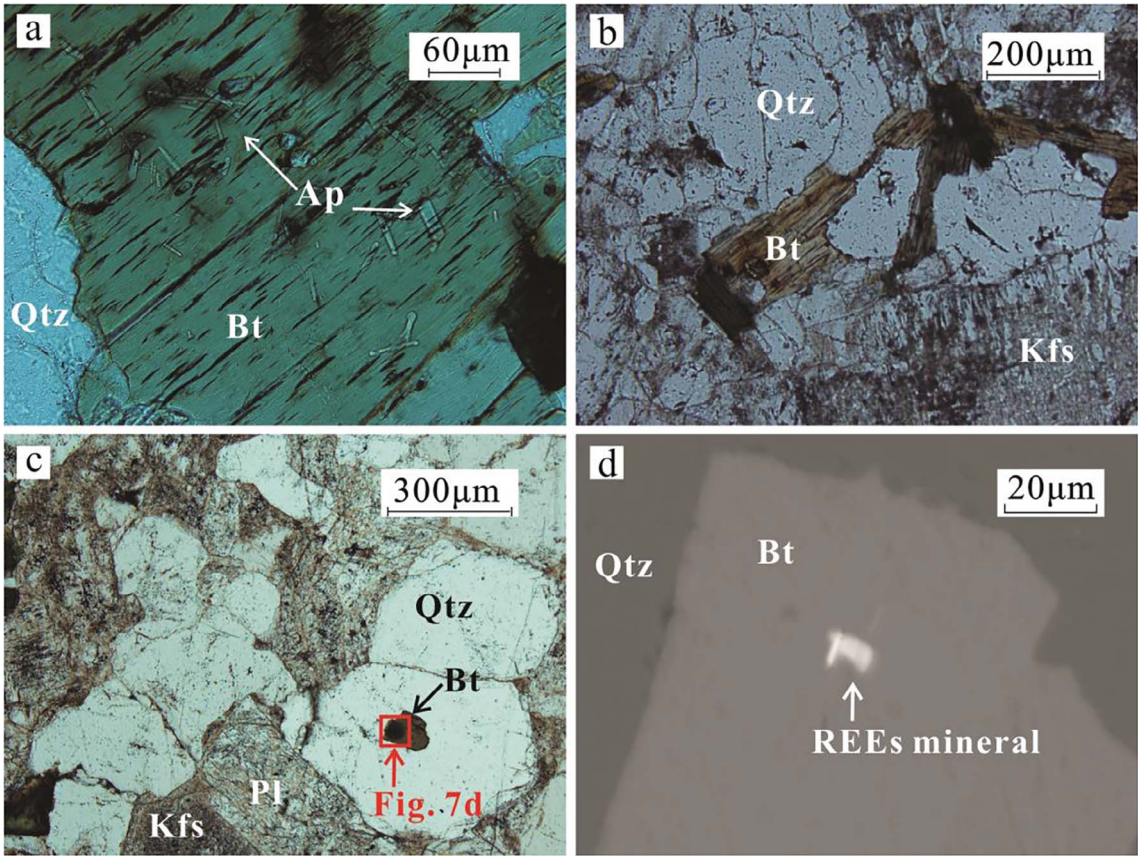

Fig. 7. Photomicrographs and BSE image of biotite in rocks of Phases I, III and IV of the Jiulongnao complex. (a) Ferribiotite with small apatite inclusions in Phase I granites, (plain polarized light, PPL); (b) Anhedral ferribiotite filling spaces between quartz and feldspar in Phase III granites, (PPL); (c) Small inclusion of siderophyllite in quartz in Phase IV granites, (PPL); (d) Siderophyllite with inclusions of rare earth mineral. Ap-Apatite; Bt-Biotite; Chl-Chlorite; Kfs-K-feldspar; Pl-Plagioclase; Qtz-Quartz.

Table 6
FsLA-ICP-MS analyse (ppm) of biotite in granites of the Jiulongnao complex.

Rock Type	Phase I				Phase II		Phase III				Phase IV			
Spots	JLN-22-1-3	JLN-22-3-1	JLN-22-3-2	JLN-22-3-3	DYL601-180-1-1-1	DYL601-180-1-2-1	JLN-1-3-1	JLN-13-10-1	JLN-13-3-3	JLN-13-3-4	JLN-6-10-1	JLN-16-1-4	JLN-16-2-4-1 included in quartz	JLN-16-2-4-2
Rb	1492	890	2444	2122	913	1785	1430	2135	771	770	5199	5547	2722	3157
Sr	14	5	3	4	9	13	14	5	22	14	7	10	11	7
Y	23	5	3	31	2	2	5	90	237	97	102	22	6499	13
Nb	167	271	269	329	168	234	371	373	238	339	462	420	7467	403
Mo	l.d.l.	l.d.l.	1	1	4	2	1	l.d.l.	l.d.l.	l.d.l.	1	l.d.l.	3	1
Sn	292	399	345	423	426	462	150	166	100	154	525	412	114	126
Cs	145	127	132	117	66	86	92	174	64	90	739	1667	151	155
Ba	85	718	10	549	3791	56	360	188	438	1416	11	27	12	8
La	9	1	1	4	2	3	10	36	184	83	1	5	13	l.d.l.
Ce	9	1	1	10	3	5	14	41	52	31	3	7	60	1
Pr	3	l.d.l.	l.d.l.	3	l.d.l.	1	2	11	39	21	l.d.l.	1	17	l.d.l.
Nd	14	2	1	15	2	2	9	47	150	74	2	7	158	1
Sm	5	1	l.d.l.	6	l.d.l.	l.d.l.	1	15	33	20	2	4	234	1
Eu	l.d.l.	l.d.l.	l.d.l.	l.d.l.	l.d.l.	l.d.l.	l.d.l.	1	3	2	l.d.l.	l.d.l.	l.d.l.	l.d.l.
Gd	5	1	l.d.l.	8	l.d.l.	l.d.l.	1	15	31	14	3	4	519	1
Tb	1	l.d.l.	l.d.l.	1	l.d.l.	l.d.l.	l.d.l.	3	6	3	2	1	136	l.d.l.
Dy	4	1	l.d.l.	7	l.d.l.	l.d.l.	1	19	37	21	19	4	1088	2
Ho	1	l.d.l.	l.d.l.	1	l.d.l.	l.d.l.	l.d.l.	4	8	4	7	1	294	1
Er	2	1	l.d.l.	3	l.d.l.	l.d.l.	1	8	23	11	33	2	782	2
Tm	l.d.l.	l.d.l.	l.d.l.	l.d.l.	l.d.l.	l.d.l.	l.d.l.	2	4	2	6	l.d.l.	120	l.d.l.
Yb	2	l.d.l.	l.d.l.	2	l.d.l.	l.d.l.	l.d.l.	8	27	15	71	2	723	3
Lu	l.d.l.	l.d.l.	l.d.l.	l.d.l.	l.d.l.	l.d.l.	l.d.l.	1	4	2	11	l.d.l.	98	l.d.l.
Ta	61	80	99	85	10	59	59	56	37	47	246	524	801	80
W	5	2	4	5	2	2	5	7	4	6	53	35	452	7
Bi	2	1	l.d.l.	1	l.d.l.	l.d.l.	l.d.l.	l.d.l.	l.d.l.	l.d.l.	13	1	2	l.d.l.
Pb	17	16	11	13	10	9	26	49	351	205	117	31	44	15
Th	2	1	2	2	l.d.l.	1	8	2	10	5	8	5	1266	1
U	1	1	1	l.d.l.	l.d.l.	l.d.l.	1	2	13	25	4	1	5608	1

l.d.l.: lower than detection limits.

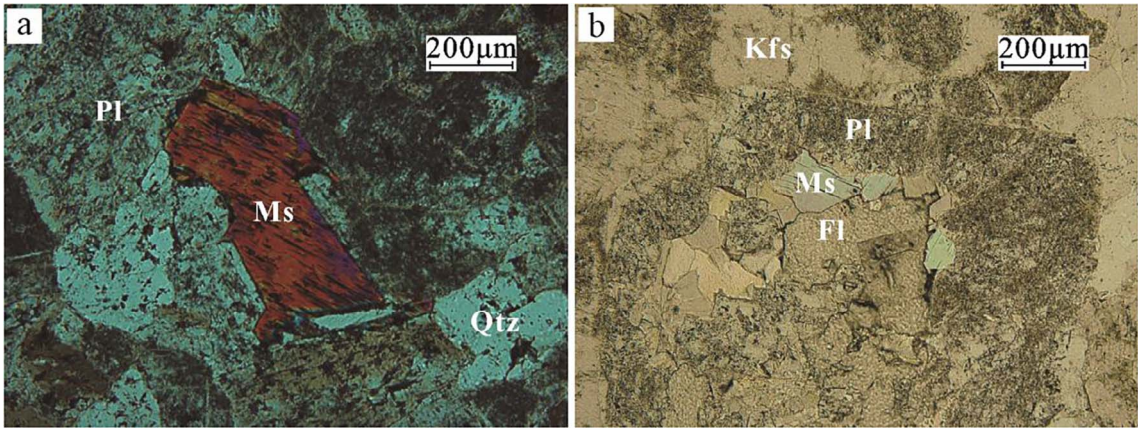

Fig. 8. Photomicrographs of muscovite in rocks of Phases II and IV from the Jiulongnao complex. (a) Primary muscovite in granites of Phase IV, (crossed nicols); (b) Secondary muscovite replacing plagioclase in granites of Phase II, (PPL). Fl-Fluorite; Kfs-K-feldspar; Ms-Muscovite; Pl-Plagioclase; Qtz-Quartz.

feldspar and quartz in granites of Phases I and II (Fig. 7a). In Phases III and IV, it occurs only as an interstitial mineral (Fig. 7b). Less common are small, euhedral inclusions of biotite in quartz of Phase IV (Fig. 7c). Major element compositions of biotite are presented in Guo et al. (2017). Fs-LA-ICP-MS analyses of trace elements are listed in Table 6. Biotite from granites of Phases I and III is ferribiotite. Biotite from granites of Phases II and IV is siderophyllite, whereas biotite of Phase IV is aluminium-rich (Guo et al., 2017). The total REE contents of biotite from granites of Phases I-IV are 5–61 ppm, 8–12 ppm, 40–599 ppm and 12–4243 ppm, respectively. The significantly high total REE of biotite from sample JLN-16-2-4-1 of Phase IV was dues to micro-inclusion of rare earth minerals (Fig. 7d). Most grains have relatively high Rb contents, up to > 5000 ppm in Phase IV granites. Nb is also relatively high and generally increases from Phase I to Phase IV.

Table 7
FsLA-ICP-MS analyse (ppm) of muscovite in granites of the Jiulongnao complex.

Rock Type	Phae II				Phase IV
Spot	DYL601-180-1-2-2	DYL601-180-1-2-3	DYL601-180-1-6-3	DYL601-180-1-6-4	JLN-6-11
Occurrence	Primary Ms		Secondary Ms		Primary Ms
Li	2349	1709	1083	1190	2995
Rb	1996	1675	2377	2381	4102
Sr	13	17	10	7	11
Y	1	2	1	1	5
Nb	47	32	36	35	39
Mo	l.d.l.	l.d.l.	l.d.l.	l.d.l.	l.d.l.
Sn	368	339	365	332	254
Cs	127	129	129	150	287
Ba	78	90	76	84	11
La	3	3	1	1	1
Ce	4	6	2	2	1
Pr	l.d.l.	l.d.l.	l.d.l.	l.d.l.	l.d.l.
Nd	1	2	1	l.d.l.	1
Sm	l.d.l.	l.d.l.	l.d.l.	l.d.l.	l.d.l.
Eu	l.d.l.	l.d.l.	l.d.l.	l.d.l.	l.d.l.
Gd	l.d.l.	l.d.l.	l.d.l.	l.d.l.	l.d.l.
Tb	l.d.l.	l.d.l.	l.d.l.	l.d.l.	l.d.l.
Dy	l.d.l.	l.d.l.	l.d.l.	l.d.l.	1
Ho	l.d.l.	l.d.l.	l.d.l.	l.d.l.	l.d.l.
Er	l.d.l.	l.d.l.	l.d.l.	l.d.l.	1
Tm	l.d.l.	l.d.l.	l.d.l.	l.d.l.	l.d.l.
Yb	l.d.l.	l.d.l.	l.d.l.	l.d.l.	2
Lu	l.d.l.	l.d.l.	l.d.l.	l.d.l.	l.d.l.
Ta	12	11	9	12	9
W	21	22	15	14	16
Bi	l.d.l.	l.d.l.	l.d.l.	l.d.l.	l.d.l.
Pb	7	7	7	7	17
Th	1	1	1	l.d.l.	1
U	l.d.l.	l.d.l.	l.d.l.	l.d.l.	l.d.l.

l.d.l.: lower than detection limits.

4.5.2. Muscovite

There are two types of muscovite in the granites of the Jiulongnao complex: (1) primary muscovite, and (2) secondary muscovite. The primary grains occur in rocks of Phases II and IV, where they occur along the margins of ferribiotite grains or as intergranular grains among feldspar crystals (Fig. 8a). The secondary muscovite replaces feldspar (Fig. 8b).

The primary muscovite is characterized by high Al_2O_3, FeO and K_2O and very low TiO_2 and MgO, whereas the secondary grains have higher Al_2O_3 and distinctly lower FeO (Guo et al., 2017). Total REE contents and most trace elements, except for Li, Rb, Ba and Cs are very low in both varieties (Table 7).

4.5.3. Plagioclase

Plagioclase in the granites of Phases I, II and IV is all albite with compositions of $Ab_{98\text{-}90}An_{1\text{-}10}Or_{0\text{-}1}$, whereas that in Phase III is mostly more calcic oligoclase with compositions of $Ab_{89\text{-}78}An_{11\text{-}20}Or_{1\text{-}10}$, accompanied by a few grains of albite (Guo et al., 2017). Total REE contents of the plagioclase in granites of Phases I to IV are 16–17 ppm, 21–25 ppm, 10–44 ppm and 7–59 ppm, respectively, and δEu values are 0.54–5.57, 0.39–0.72, 0.47–6.28 and 0.20–0.24, respectively. Both Rb and Sr contents are low except in grains from Phase III (Table 8).

4.5.4. K-feldspar

The K-feldspars in the granites of the Jiulongnao complex include both orthoclase and microcline, whose major element compositions are similar in all four phases (Guo et al., 2017). Rb contents are relatively high in all the grains and generally increase from Phase I to Phase IV with a maximum of 1900 ppm, but Sr contents are all < 100 ppm. Ba reaches a maximum of 575 ppm in rocks of Phase III and is lower in the other rocks (Table 8).

4.5.5. Garnet

Garnet is present only in the rocks of Phase IV, where it occurs as euhedral grains from 0.3 to 1.5 mm across. Textural relationships indicate that it crystallized before quartz, feldspar and siderophyllite,

Table 8
FsLA-ICP-MS analyse (ppm) of feldspar in granites of the Jiulongnao complex.

Rock Type	Phase I				Phase II					Phase III					Phase IV				
Spot	JLN-22-1-1	JLN-22-4-4	JLN-22-4-2	JLN-22-4-3	DYL601-180-1-3-4	DYL601-180-1-5-3	DYL601-180-1-3-3	DYL601-180-1-5-2	DYL601-180-1-6-2	JLN-13-4-1	JLN-1-1-2	JLN-1-2-1	JLN-13-2-1	JLN-13-9-2	JLN-6-10-3	JLN-16-2-3	JLN-6-10-2	JLN-16-1-3	JLN-16-2-2
Mineral	Kfs	Kfs	Pl	Pl	Kfs	Kfs	Pl	Pl	Pl	Kfs	Pl	Pl	Pl	Pl	Kfs	Kfs	Pl	Pl	Pl
Rb	420	1041	26	20	715	750	8	9	42	822	95	11	8	165	1725	1909	124	7	11
Sr	68	30	54	30	23	23	21	19	57	99	230	75	71	151	12	19	14	43	22
Y	3	5	1	5	1	1	1	4	9	15	4	1	1	5	18	1	28	2	1
Zr	17	5	2	22	41	34	14	18	20	3	12	11	11	17	11	8	12	9	14
Nb	1	l.d.l.	l.d.l.	1	l.d.l.	l.d.l.	1	1	l.d.l.	27	10	1	38	2	1	1	11	1	1
Mo	1	2	l.d.l.	1	1	2	l.d.l.	l.d.l.	l.d.l.	l.d.l.	l.d.l.	1	1	l.d.l.	l.d.l.	l.d.l.	l.d.l.	1	l.d.l.
Sn	1	3	1	2	1	2	3	3	2	6	3	1	2	3	4	2	8	1	2
Cs	8	7	1	1	4	23	l.d.l.	1	2	8	7	l.d.l.	l.d.l.	10	20	67	11	l.d.l.	l.d.l.
Ba	202	28	4	18	89	72	24	30	34	575	131	13	54	155	8	50	7	23	16
La	2	1	1	4	4	12	7	4	7	9	12	7	3	13	2	2	2	4	2
Ce	3	1	3	6	6	14	11	7	8	5	8	10	4	16	2	2	3	5	3
Pr	l.d.l.	l.d.l.	12	1	1	1	1	1	1	2	1	1	l.d.l.	3	l.d.l.	l.d.l.	l.d.l.	1	l.d.l.
Nd	1	1	1	3	2	11	3	3	4	8	5	2	2	7	1	1	2	2	1
Sm	l.d.l.	l.d.l.	l.d.l.	1	l.d.l.	2	l.d.l.	1	1	2	1	l.d.l.	l.d.l.	1	l.d.l.	l.d.l.	l.d.l.	1	l.d.l.
Eu	l.d.l.	l.d.l.	l.d.l.	l.d.l.	l.d.l.	l.d.l.	l.d.l.	l.d.l.	l.d.l.	1	l.d.l.	1	l.d.l.	1	l.d.l.	l.d.l.	l.d.l.	l.d.l.	l.d.l.
Gd	1	l.d.l.	l.d.l.	1	l.d.l.	1	l.d.l.	2	1	3	1	l.d.l.	l.d.l.	1	l.d.l.	l.d.l.	1	l.d.l.	l.d.l.
Tb	l.d.l.	l.d.l.	l.d.l.	l.d.l.	l.d.l.	l.d.l.	l.d.l.	l.d.l.	l.d.l.	l.d.l.	l.d.l.	l.d.l.	l.d.l.	l.d.l.	l.d.l.	l.d.l.	l.d.l.	l.d.l.	l.d.l.
Dy	l.d.l.	l.d.l.	l.d.l.	1	l.d.l.	l.d.l.	l.d.l.	2	1	3	l.d.l.	l.d.l.	l.d.l.	1	3	l.d.l.	6	l.d.l.	l.d.l.
Ho	l.d.l.	l.d.l.	l.d.l.	l.d.l.	l.d.l.	l.d.l.	l.d.l.	l.d.l.	l.d.l.	1	l.d.l.	l.d.l.	l.d.l.	l.d.l.	2	l.d.l.	2	l.d.l.	l.d.l.
Er	l.d.l.	l.d.l.	l.d.l.	l.d.l.	l.d.l.	l.d.l.	l.d.l.	1	1	2	l.d.l.	l.d.l.	l.d.l.	l.d.l.	6	l.d.l.	11	l.d.l.	l.d.l.
Tm	l.d.l.	l.d.l.	l.d.l.	l.d.l.	l.d.l.	l.d.l.	l.d.l.	l.d.l.	l.d.l.	l.d.l.	l.d.l.	l.d.l.	l.d.l.	l.d.l.	1	l.d.l.	3	l.d.l.	l.d.l.
Yb	l.d.l.	l.d.l.	l.d.l.	l.d.l.	l.d.l.	l.d.l.	l.d.l.	1	1	1	l.d.l.	l.d.l.	l.d.l.	1	15	l.d.l.	25	l.d.l.	l.d.l.
Lu	l.d.l.	l.d.l.	l.d.l.	l.d.l.	l.d.l.	l.d.l.	l.d.l.	l.d.l.	l.d.l.	l.d.l.	l.d.l.	l.d.l.	l.d.l.	l.d.l.	2	l.d.l.	3	l.d.l.	l.d.l.
Ta	l.d.l.	l.d.l.	l.d.l.	l.d.l.	l.d.l.	l.d.l.	l.d.l.	l.d.l.	l.d.l.	4	2	l.d.l.	2	l.d.l.	l.d.l.	l.d.l.	6	l.d.l.	l.d.l.
W	l.d.l.	l.d.l.	l.d.l.	l.d.l.	l.d.l.	l.d.l.	l.d.l.	l.d.l.	l.d.l.	l.d.l.	l.d.l.	l.d.l.	l.d.l.	l.d.l.	l.d.l.	1	1	l.d.l.	l.d.l.
Bi	3	l.d.l.	l.d.l.	l.d.l.	l.d.l.	l.d.l.	l.d.l.	l.d.l.	l.d.l.	l.d.l.	l.d.l.	l.d.l.	l.d.l.	l.d.l.	l.d.l.	l.d.l.	l.d.l.	l.d.l.	l.d.l.
Pb	33	104	17	23	73	80	54	56	13	110	13	28	28	21	179	131	52	47	26
Th	1	2	l.d.l.	2	1	4	l.d.l.	8	l.d.l.	4	3	1	1	8	1	1	2	2	1
U	1	l.d.l.	l.d.l.	1	l.d.l.	13	l.d.l.	98	l.d.l.	3	1	l.d.l.	l.d.l.	1	18	l.d.l.	1	1	1

l.d.l.: lower than detection limits.

indicating its magmatic origin (Fig. 9a-b). It consists of approximately equal amounts of almandine (42.18–47.18 M%) and spessartine (51.09–55.71 M%) (Guo et al., 2017), thus resembling garnets from the Xihuashan granites, and those occurring in rare-metal granitic pegmatites (Wang et al., 2003; Yang et al., 2013). The grains are clearly zoned with high contents of total REE, W, U, Nb and Ta of 10739, 106, 64, 1144 and 227 ppm, respectively, all of which are strongly depleted in the rims (Table 9) (Fig. 9c-d).

4.5.6. Fergusonite

Fergusonite occurs as discrete crystals in granites of Phases I and II and commonly in Phase IV. It forms micro-inclusions (15–100 μm) in quartz, siderophyllite, feldspar and garnet, and in some cases, coexists with uraninite (Fig. 10c-d). Niobium is a major constituent in this mineral, ranging from 39.19 to 47.58 wt% Nb_2O_5 and 1.52–8.77 wt% Ta_2O_5. In addition, the fergusonite contains 0.62–4.03 wt% WO_3, 0.47–2.38 wt% ThO_2, and 0.89–3.96 wt% UO_2 (Table 10).

4.5.7. Uraninite

Uraninite occurs in granites of all four phases, where it appears in three different modes: (1) as euhedral-subhedral grains (~100 μm) in siderophyllite (Fig. 10a); (2) as micro-inclusions in feldspar, zircon or fergusonite (5–25 μm) (Fig. 10d); and (3) intergrown with zircon (~20 μm) (Fig. 10b). The uraninite has UO_2 contents of 47.41–56.24 wt %, ThO_2 contents of 5.15–8.98 wt%, PbO contents of 1.37–1.72 wt%, Dy_2O_3 contents of 0.79–1.29 wt% and Y_2O_3 contents of 4.00–7.56 wt% (Table 11). The high contents of Th suggest that the uraninite crystallized in equilibrium with uranium-bearing thorite (Wang et al., 2003). Because U is a large ion lithophile element, it rarely substitutes for other elements in ore-forming minerals. Thus, the relative abundance of uraninite in these granites indicates enrichment of U in their parental magmas.

4.5.8. Pyrochlore

Pyrochlore is only found in granites of Phase IV, where it is associated with siderophyllite. It forms small (~40 μm), euhedral crystals that commonly display compositional zonation in BSE images (Fig. 10e). The pyrochlore compositions are dominated by Nb_2O_5 (28.44–30.32 wt%), Ta_2O_5 (10.77–15.55 wt%), and PbO (1.53–24.95 wt%), but most grains also contain small amounts of UO_2, ThO_2, Y_2O_3, WO_3, and SnO_2. Most grains are zoned with decreasing Nb, Ta, Pb, Th, U and Sn contents and increasing W and Y from core to rim (Table 12).

4.5.9. Ilmenite, rutile and cassiterite

Ilmenite occurs only in granites of Phase III, where it has two modes of occurrence: (1) euhedral grains included in feldspar (Fig. 10f) and (2) sheet-like inclusions in chloritized ferribiotite. The ilmenite consists mainly of TiO_2, FeO and MnO, with small amounts of Nb, Ta, Sn, and W (Guo et al., 2017).

Rutile occurs only in granites of Phase IV where it forms grains ~50 μm across, and is accompanied by chlorite, zircon and fergusonite (Fig. 10 g). It consists chiefly of TiO_2, FeO and Nb_2O_5 with small amounts of Ta_2O_5, WO_3 and SnO_2 (Table 13).

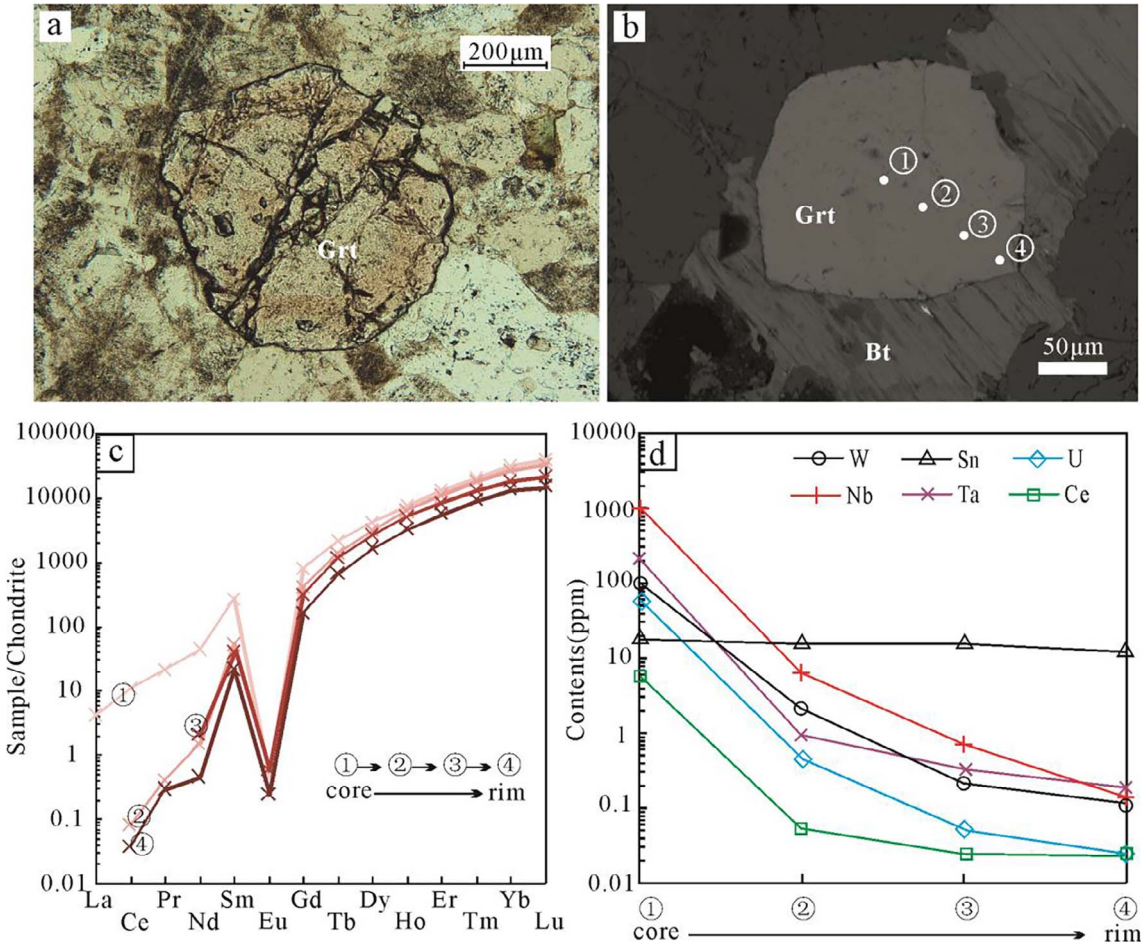

Fig. 9. Photomicrograph, BSE image and compositional diagrams of garnets in rocks of Phase IV. (a) Photomicrograph of garnet, (PPL); (b) BSE image of garnet and biotite; (c) Chondrite-normalized REE patterns of garnet in (b), showing strong enrichment in HREE and depletion in LREE. Also shown are core-rim variations in REE contents; d) Diagram showing variations of W, Sn, U, Nb, Ta and Ce contents of the garnet grain in (b).

A few very small (~10 μm) grains of cassiterite have been found in granites of Phase IV, accompanied by siderophyllite (Fig. 10 h). It consist of SnO_2 (> 90 wt%) and minor FeO, Nb_2O_5 and Ta_2O_5 (Table 13). Its FeO content is lower than that of cassiterite in the Huashan tin granite (2.16 wt%), whereas the Nb_2O_5 and Ta_2O_5 contents are higher (Wang et al., 2012).

5. Discussion

5.1. Ages of the Jiulongnao complex

Guo (2010) and Feng et al. (2011a) previously reported the formation age of the Jiulongnao complex as 154.9 Ma and 155.8 Ma, respectively. However, the dated samples were from one phase, leaving unclear the age spectrum of the complex. In this study, precise LA-ICP-MS zircon U-Pb dating shows that the four phases of the complex (Phases I to IV) were emplaced at 160.9 ± 0.6 Ma, 158.6 ± 0.7 Ma, 157.0 ± 1.5 Ma and 154.1 ± 1.2 Ma, respectively, similar to the ages of W-mineralized granites elsewhere in southern Jiangxi Province (Feng et al., 2007; Liu et al., 2007; Feng et al., 2011b; Guo et al., 2011b, 2012; Fang et al., 2014). Numerous mineralization ages for these granites have also been obtained recently (Table 14). These new data suggest that the major W-dominated polymetallic mineralization occurred between 157 and 150 Ma in southern Jiangxi Province (Feng et al., 2007, 2011a; Zeng et al., 2009, 2011; Guo et al., 2011b; Wang et al., 2011; Li et al., 2014; Wang et al., 2017a,b), without a distinct time gap between the mineralization and related granitic magmatism.

5.2. Petrogenesis of the Jiulongnao complex

Mineral assemblages and compositions record magma compositions, and can be used to study the nature of magma sources. The Jiulongnao granites have primary muscovite, ilmenite and magmatic garnet. Ferribiotie and siderophyllite have low MgO contents (0.28–4.59 wt%) and $Mg^{\#}$ values (0.02–0.22, which are lower than typical $Mg^{\#}$ values (0.4) for biotite from S-type granites (Whalen and Chappell, 1988). Moreover, all the granites have relatively high K_2O/Na_2O ratios (1.04–2.38, which is higher than the values (< 1.0) of I-type granites (Chappell, 1999; Chappell et al., 2012). Most of the granites are peraluminous, with only a few metaluminous samples. These data indicate that the Jiulongnao granites are S-type, as indicated in Fig. 11.

Ferribiotite and siderophyllite in the granites has low MgO and high FeO, a feature of crust-derived granites elsewhere in South China (Guo et al., 2017). The $\varepsilon_{Nd}(t)$ values of the granites all plot in the field of Precambrian crust of South China (Fig. 12b), and most zircons plot in the area between upper and lower crust (Fig. 12a). Geochemical characteristics of minerals (i.e. biotie and zircon) and whole-rock data indicate a crustal origin. The two-stage Hf model ages are 1.7–2.3 Ga,

Table 9
FsLA-ICP-MS analyse (ppm) of garnet in Phase IV granites of the Jiulongnao complex.

Spot	JLN-6-7-1	JLN-16-8			
		①	②	③	④
Rb	4	2	2	2	1
Sr	2	2	2	1	1
Y	6711	14,434	11,150	7723	3450
Zr	2	6	3	3	1
Nb	l.d.l.	1144	7	1	l.d.l.
Mo	l.d.l.	1	1	l.d.l.	1
Sn	28	18	16	16	12
Cs	l.d.l.	l.d.l.	l.d.l.	l.d.l.	l.d.l.
Ba	1	l.d.l.	l.d.l.	l.d.l.	l.d.l.
La	l.d.l.	1	l.d.l.	l.d.l.	l.d.l.
Ce	l.d.l.	7	l.d.l.	l.d.l.	l.d.l.
Pr	l.d.l.	2	l.d.l.	l.d.l.	l.d.l.
Nd	1	21	1	1	l.d.l.
Sm	9	41	8	6	3
Eu	l.d.l.	l.d.l.	l.d.l.	l.d.l.	l.d.l.
Gd	99	166	85	66	33
Tb	66	82	51	44	25
Dy	999	1070	790	691	415
Ho	395	429	349	289	183
Er	1799	2150	1786	1393	939
Tm	422	530	454	343	234
Yb	3832	5245	4466	3221	2260
Lu	646	996	830	553	378
Ta	l.d.l.	227	1	l.d.l.	l.d.l.
W	l.d.l.	106	2	l.d.l.	l.d.l.
Bi	l.d.l.	l.d.l.	l.d.l.	l.d.l.	l.d.l.
Pb	2	1	1	l.d.l.	l.d.l.
Th	l.d.l.	31	5	l.d.l.	l.d.l.
U	l.d.l.	64	l.d.l.	l.d.l.	l.d.l.

l.d.l.: lower than detection limits.

suggesting that the granites formed by partial melting of Paleo-Proterozoic crust.

5.3. Physicochemical conditions of the parental magmas

Silicate minerals in granites have important implications for variations in physical and chemical conditions, such as temperature, oxygen fugacity and pressure, during magmatic evolution (Zhao et al., 2005). The $Fe^{3+}/(Fe^{2+}+Fe^{3+})$ ratios of biotite from Phases I to IV are 0.09–0.12, 0, 0–0.09, and 0–0.27, respectively. Ferribiotite of Phase I plots around the oxygen buffer line of Ni-NiO, in the Fe^{3+}-Fe^{2+}-Mg triangular diagram, whereas siderophyllite trapped in quartz of Phase IV plots around the line between Fe_2O_3-Fe_3O_4, and others plot below the line of Fe_2SiO_4-SiO_2-Fe_3O_4 (Guo et al., 2017). These observations indicate that granites of Phases I to III crystallized under low oxygen fugacity, whereas early Phase IV varieties crystallized under high oxygen fugacity, but that the oxygen fugacity decreased in the later stages. The presence of cassiterite in the rocks of Phase IV, supports the interpretation of high oxygen fugacity in the early stages (Pichavant et al., 1996).

On the basis of whole-rock composition, we have obtained zircon saturation temperatures (T_{Zr}) of 746–760 °C, 712–802 °C, 798–810 °C, and 648–731 °C for Phases I to IV, respectively. These temperatures approximately represent the maximum temperature of the magma (Watson and Harrison, 1983; Miller et al., 2003).

The different oxidation state and temperature of the granite may be a consequence of different magma sources (Oyarzun et al., 2001; Mungall, 2002; Sato, 2012; Romer and Kroner, 2016) and/or different paths of magma evolution (Sun et al., 2004; Lee et al., 2010; Trail et al., 2012). During the Early Mesozoic, the tectonic setting of East Asia switched from the Tethyan tectonic domain to the Paleo-Pacific tectonic domain (Yang et al., 1998; Shu et al., 2006; Shu, 2012; Ji et al., 2017). NE- and NNE-trending deep fractures developed in South China. The Jiulongnao complex is situated between the NNE-trending Ganjiang and Yingtan-Anyuan deep faults (Chen et al., 1989). Emplacement of the Jiulongnao complex was obviously controlled by these faults, especially the granites of Phases III and IV, which are located at the intersections of NE-trending faults and NNE-, NW- NS-trending secondary ones (Fig. 2). Deep fractures resulted in re-melting of basic materials in the lower crust, some proportion of which might be involved in the formation of granites of later phases. The high $\varepsilon_{Hf}(t)$ values of inherited zircon grains in granites of Phase IV support a change of magma sources. Such a change might be cause for the fluctuation of oxygen fugacity and temperature.

5.4. Highly fractionated magma and associated W-Sn-U-Nb-Ta mineralization

Plagioclase in Phases I, II and IV is dominated by albite. Biotite has ferribiotite-siderophyllie compostions, with *MF* values of 0.0230–0.2195, similar to biotite of the Xihuashan granites (Guo et al., 2012, 2017). Muscovite is rich in iron, with $Mg^{\#}$ values of 0.21–0.23. Spessartine-almandine in rocks of Phase IV, with a small amount of Nb, is similar to garnet in the Xihuashan granites and in rare metal-bearing pegmatite (Wang et al., 2003; Yang et al., 2013). This type of garnet usually crystallizes from magmatic-hydrothermal fluids during crystal fractionation (Tan, 1984). The assemblages and compositions of rock-forming minerals in the Jiulongnao granites are similar to those of granites related to W-dominated polymetallic deposits in South China (Guo et al., 2014).

Granites of the Jiulongnao complex display remarkably Eu, Ba, Nb, Sr, P and Ti negative anomalies, implying that the magmas underwent intense fractional crystallization. Fractional crystallization of plagioclase and quartz in evolved melts will increase such elements as W, Sn, Nb, Ta and U. Experiments have demonstrated that low oxygen fugacity can promote the accumulation of W in hydrothermal fluids (Candela and Bouton, 1990; Bali et al., 2012), whereas the solubility of cassiterite in granitic melts would decrease with increased of oxygen fugacity. Thus, primary cassiterite in the granite of Phase IV is a direct indicator of high oxygen fugacity conditions (Pichavant et al., 1996). Uranium in magma can occur in three different states, namely U^{4+}, U^{5+}, and U^{6+}, depending on the oxygen fugacity conditions (Calas, 1979). Uranium would be dissolved and transported in the melts with high oxidation states and would be deposited under reducing conditions. Thus, different mineral associations can be used to estimate the oxygen fugacity of parental melts. Considering the geological features of W-dominated polymetallic deposits around Phases I and II of the Jiulongnao complex (Fig. 2), the ages of mineralization (151.1–158.8 Ma), the increasing W concentrations of the granites from Phases I to IV (Table 4), and scheelite in the granite (Wang et al., 2017a), we suggest that W mineralization took place between the post-magmatic stage of Phase I and the end of Phase IV. Low oxygen fugacities during Phases I and II produced dominantly U^{4+}, which was advantageous for crystallization of uraninite. Only sporadic uraninite crystallized during Phase I, indicating that U accumulation was weak, but as the magma evolved, more uraninite and thorite were formed and Nb mineralization was initiated, as indicated by the appearance of fergusonite in rocks of Phase II. In the late stage of crystallization (Phase IV), the oxygen fugacity varied from high to low. High oxygen fugacity resulted in U being included in pyrochlore in the form of U^{6+} (Lumpkin et al., 1986), resulting in weak U mineralization. At the same time, W^{6+} substituted for Ti^{4+} in rutile bringing large quantities of W^{6+} into this mineral. EPMA analyses show that W contents are up to 1.4% WO_3 wt% in rutile

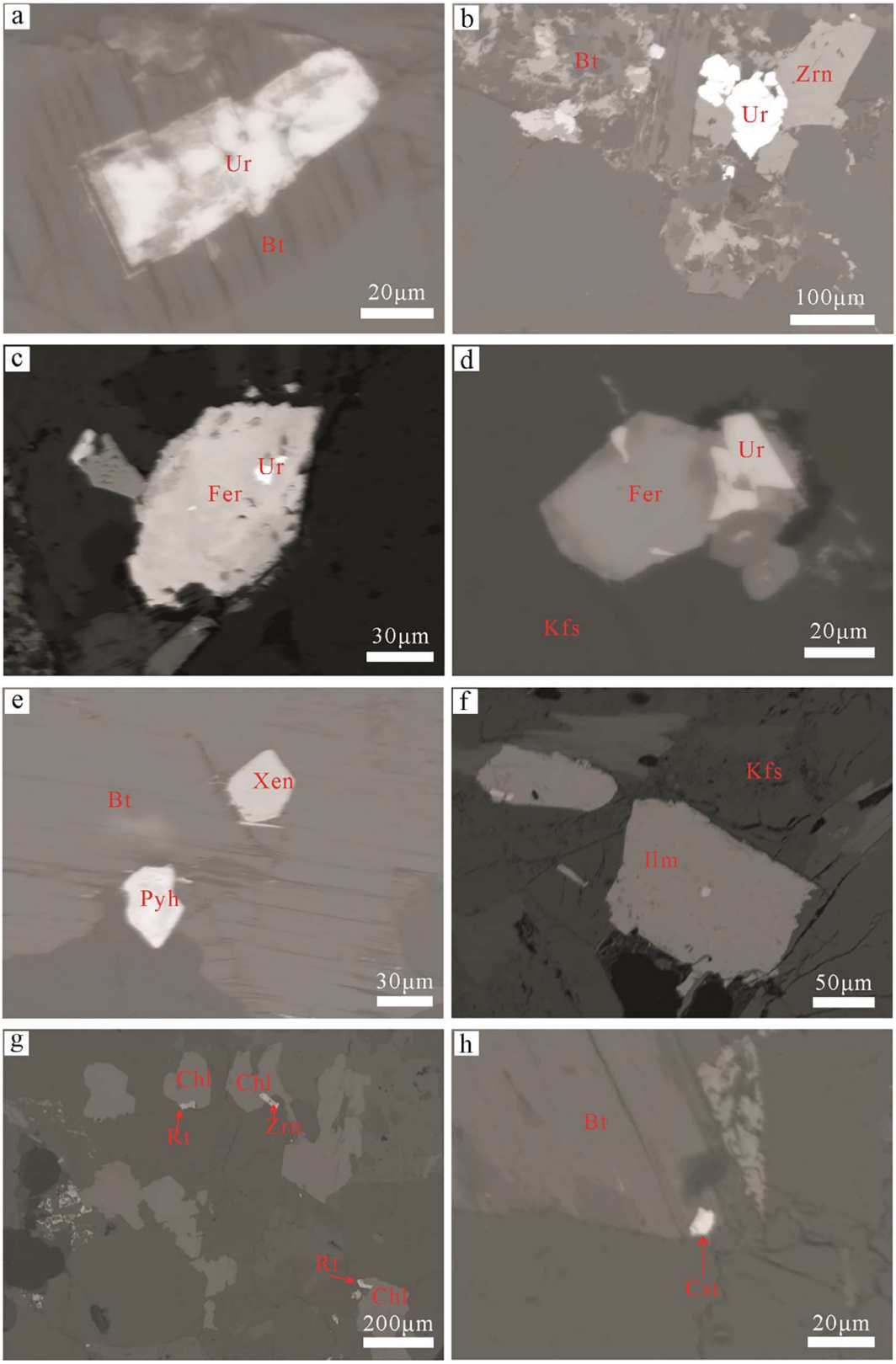

Fig. 10. BSE images of accessory minerals in granites of the Jiulongnao complex. (a) Uraninite in biotite; (b) Uranium minerals included in altered biotite; (c)-(d) Fergusonite containing or accompanying uraninite; (e) Xenotime and pyrochlore included in biotite; (f) Ilmenite with K-feldspar; (g) Rutile with chlorite; (h) Cassiterite included in biotite. Bt-Biotite; Chl-Chlorite; Cst-Cassiterite; Fer-Fergusonite; Kfs-K-feldspar; Pyh-Pyrochlore; Rt-Rutile; Ur-Uraninite; Xen-Xenotime; Zrn-Zircon.

Table 10
EPMA analyse (wt%) of fergusonite in granites of the Jiulongnao complex.

Rock type	Phase I	Phase II		Phase IV				
Spot	JLN-22-4-8	DYL601-180-1-5-7	DYL601-180-1-5-8	JLN-16-4-4-1	JLN-16-4-4-4	JLN-16-4-4-5	JLN-6-7-3	JLN-6-9-2
Occurrence	Enclosed in biotite	Enclosed in K-feldspar	Enclosed in K-feldspar	Coexists with zircon	Enclosed in biotite	Enclosed in biotite	Enclosed in garnet	Enclosed in quartz
SiO_2	0.27	7.21	0.17	2.30	2.01	0.21	l.d.l.	3.01
CaO	0.25	6.00	0.47	1.20	1.70	0.72	0.39	0.95
FeO	1.29	0.91	0.04	0.29	0.13	0.00	0.46	0.01
Nb_2O_5	45.49	47.13	47.58	39.19	39.34	42.75	43.30	44.38
Ta_2O_5	2.49	2.50	1.52	8.14	4.45	8.77	5.93	2.81
WO_3	0.62	0.96	1.43	2.51	4.03	1.15	1.21	0.84
SnO_2	l.d.l.	0.04	l.d.l.	0.01	l.d.l.	l.d.l.	l.d.l.	l.d.l.
PbO	0.59	0.27	0.35	0.82	0.34	0.30	0.21	0.36
ThO_2	2.18	2.38	1.49	1.22	0.97	0.47	0.54	1.16
UO_2	0.89	3.96	1.42	0.96	0.90	0.91	1.02	3.02
La_2O_3	l.d.l.	l.d.l.	l.d.l.	l.d.l.	0.06	0.08	l.d.l.	0.06
Ce_2O_3	0.20	0.38	0.31	0.44	0.43	0.35	0.27	0.32
Pr_2O_3	0.19	l.d.l.	0.04	0.03	0.09	0.05	0.17	0.09
Nd_2O_3	1.05	0.43	0.98	0.86	0.69	0.89	0.78	0.66
Sm_2O_3	1.53	0.77	0.92	0.97	0.86	0.96	1.44	0.53
Gd_2O_3	2.92	1.09	2.72	1.43	2.14	1.97	1.61	2.08
Dy_2O_3	5.14	2.24	5.18	4.00	4.61	5.43	6.11	3.77
Ho_2O_3	1.67	0.54	1.34	1.15	1.24	1.67	1.49	1.00
Tm_2O_3	0.56	0.22	0.53	0.83	0.41	0.83	0.82	0.49
Yb_2O_3	3.02	1.35	2.05	2.87	2.68	3.48	4.91	2.41
Y_2O_3	23.78	11.72	26.23	23.20	25.58	25.28	21.40	23.52
Sc_2O_3	l.d.l.	l.d.l.	0.02	0.03	0.06	0.05	0.02	0.01
Total	94.11	90.09	94.80	92.45	92.71	96.31	92.07	91.47

l.d.l.: lower than detection limits.

Table 11
EPMA analyse (wt%) of uraninite in the granites of the Jiulongnao complex.

Rock type	Phase I	Phase II		Phase III	Phase IV	
Spot	JLN-22-3-6	DYL601-180-1-4-5	DYL601-180-1-5-9	JLN-13-12-4	JLN-16-4-4-3	JLN-16-5-4
Occurrence	Enclosed in biotite	Enclosed in biotite	Enclosed in K-feldspar	Enclosed in zircon	Enclosed in fergusonite	Coexsits with zircon
SiO_2	l.d.l.	l.d.l.	0.62	2.78	0.18	0.19
PbO	1.72	1.60	1.61	1.37	1.58	1.71
ThO_2	7.25	8.01	7.22	7.68	8.98	5.15
UO_2	56.24	55.85	55.93	47.41	52.29	54.01
La_2O_3	0.09	0.06	0.04	l.d.l.	0.05	0.02
Ce_2O_3	0.23	0.27	0.09	0.07	0.12	0.21
Pr_2O_3	0.05	0.11	l.d.l.	l.d.l.	0.07	0.14
Nd_2O_3	0.37	0.29	0.28	l.d.l.	0.37	0.13
Sm_2O_3	0.30	0.29	0.46	0.16	0.40	0.54
Gd_2O_3	0.37	0.58	0.29	l.d.l.	0.51	0.45
Dy_2O_3	1.03	0.79	1.24	1.03	1.24	1.29
Ho_2O_3	0.25	0.40	0.46	0.09	0.35	0.71
Tm_2O_3	0.03	0.15	0.27	l.d.l.	l.d.l.	0.23
Yb_2O_3	0.62	0.09	0.34	1.49	0.71	0.68
Y_2O_3	4.00	4.90	4.99	7.56	7.39	6.14
Total	72.53	73.40	73.82	69.62	74.23	71.58

l.d.l.: lower than detection limits.

from granites of Phase IV, equivalent to the value of rutile from granite of the Yichun complex (Belkasmi et al., 2000; Wang et al., 2008). Primary cassiterite also crystallized under these high oxygen fugacity conditions. Fergusonite, pyrochlore and columbite-tantalite all crystallized during Phase IV (Zhao et al., 2017b), resulting in significant accumulation of Nb and Ta in the granites.

The abundance of the ore-forming elements increased gradually during evolution of the Jiulongnao granitic magmas, but the formation of ore bodies depends on various other factors, e.g., hydrothermal activity. W-Sn-polymetallic deposits in Nanling are characterized by remarkable potassium alteration, silicification, greisenization and fluoritization (Chen et al., 1989; Liu et al., 2015; Chen et al., 2016; Legros et al., 2016; Tang et al., 2016; Xiang et al., 2017; Liu et al., 2017). In the Jiulongnao ore field, extensive greisenization and potassium alteration occur in the Xihuashan-Dangping and Taoxikeng deposits, and fluoritization is extensive in the Wayaokeng and Keshuling deposits. All of this alteration is due to post-magmatic hydrothermal fluids. Granites of Phase II have relatively high F (0.13–0.59 wt %) and Cl (89–499 ppm) consistent with the occurrence of fluorite, indicating the involvement of F-rich fluids. Ore-forming elements, including W, Sn, Nb, Ta, were transported in the form of complex compounds in the fluids, and preferentially deposited in the dome,

Table 12
EPMA analyse (wt%) of pyrochlore in Phase IV granites of the Jiulongnao complex.

Spot	JLN-16-1-6-1	JLN-16-1-6-2	JLN-16-1-6-3
	Form core (-1) to rim (-3)		
SiO_2	6.72	5.92	20.01
Al_2O_3	1.18	0.99	l.d.l.
CaO	1.58	1.69	1.05
FeO	2.23	1.88	0.53
Nb_2O_5	30.32	29.44	28.44
Ta_2O_5	15.55	15.54	10.77
WO_3	1.00	1.15	1.23
SnO_2	0.23	0.15	0.09
PbO	24.95	19.89	1.53
ThO_2	1.48	1.61	0.97
UO_2	4.12	3.38	0.89
La_2O_3	0.22	0.08	0.14
Ce_2O_3	0.32	0.44	0.37
Pr_2O_3	0.30	0.17	0.02
Nd_2O_3	0.34	0.44	0.81
Sm_2O_3	0.11	0.30	0.98
Gd_2O_3	0.25	0.43	1.72
Dy_2O_3	0.47	1.53	3.68
Ho_2O_3	l.d.l.	0.13	1.09
Tm_2O_3	0.32	0.35	0.71
Yb_2O_3	0.33	0.32	2.85
Y_2O_3	1.29	4.67	18.31
Total	93.30	90.51	96.16

l.d.l.: lower than detection limits.

Table 13
EPMA analyse (wt%) of rutile and cassiterite in granites of the Jiulongnao complex.

Mineral	Rutile			Cassiterite
Rock type	Phase IV			Phase IV
Spot	JLN-16-6-9	JLN-16-6-8	JLN-16-4-2	JLN-16-1-11
SiO_2	1.57	0.90	5.19	0.94
TiO_2	69.01	71.38	82.38	n.d.
Al_2O_3	0.74	0.70	0.39	0.19
FeO	6.74	7.22	3.40	1.87
MnO	0.20	0.17	0.12	n.d.
MgO	0.09	l.d.l.	l.d.l.	0.10
Nb_2O_5	10.41	9.91	3.90	1.33
Ta_2O_5	6.61	5.85	2.62	3.00
SnO_2	0.83	0.86	0.42	90.76
WO_3	1.42	1.36	0.50	l.d.l.
Total	97.63	98.36	98.91	98.18

l.d.l.: lower than detection limits; n.d.: not determined.

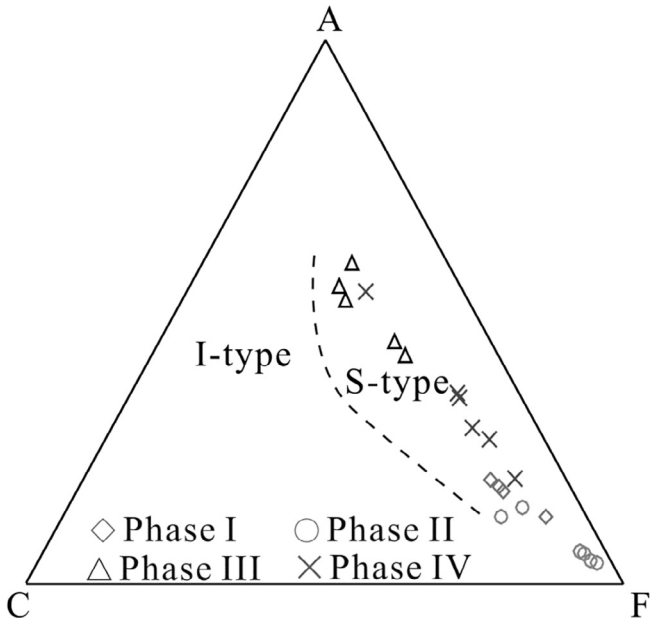

Fig. 11. ACF classification diagram for granite. A = Al_2O_3-Na_2O-K_2O (mole/%); C = CaO (mole/%); F = FeO + MgO (mole/%) (after Nakada and Takahashi, 1979). Note the systematic compositional evolution of the magmas from Phases I to IV.

transitional zone or fractures with different orientations.

6. Conclusions

(1) The Jiulongnao complex is composed of four intrusive phases (I, II, III, IV) that were emplaced at 160.9 ± 0.6 Ma, 158.6 ± 0.7 Ma, 157.0 ± 1.5 Ma and 154.1 ± 1.2 Ma, respectively. These four phases consist of S-type granites and are formed by partial melting of Paleo-Proterozoic rocks.
(2) The four phases of the Jiulongnao complex crystallized at temperatures of 746–760 °C, 712–802 °C, 798–810 °C, and 648–731 °C, respectively.
(3) Phases I, II and III crystallized under low oxygen fugacity conditions, whereas Phase IV crystallized under high oxygen fugacity in the early stage and relatively reduced fugacity in the later stage.
(4) W mineralization in the Jiulongnao area is genetically related to Phases I, II and IV, whereas U mineralization was probably closely associated with Phase II. Sn, Nb and Ta mineralization occurred during the crystallization of Phase IV.

Table 14
Representative geochronology data for W-dominated deposits and related granites in southern Jiangxi Province.

Deposit Name	Deposit Type	Method/Age(Ma)/Reference for Deposit	Ore-forming Granite	Method/Age(Ma)/Reference for Granite
Hongshuizhai	Greisen-type W	Re-Os: 156.3 ± 1.3 (Feng et al., 2011a)	Jiulongnao	U-Pb: 160.9 ± 0.6–154.1 ± 1.2
Taoxikeng	Quartz vein-type W-Sn	Re-Os: 154.4 ± 3.8 (Guo et al., 2011b)	Taoxikeng	U-Pb: 158.7 ± 3.9–157.6 ± 3.5 (Guo et al., 2011b)
Xihuashan	Quartz vein-type W	Re-Os: 157.0 (Wang et al., 2011)	Xihuashan	U-Pb: 161 ± 3 ~ 158 ± 2 (Guo et al., 2012)
Zhangdongkeng	Quartz vein-type W	Re-Os: 151.1 ± 1.2 (Li et al., 2014) Re-Os: 151.3 ± 1.7 (Li et al., 2014)	Jiulongnao	U-Pb: 160.9 ± 0.6–154.1 ± 1.2
Meishuping	Quartz vein-type W-Mo	Re-Os: 156.2 ± 0.93 (Wang et al., 2017a)	Jiulongnao	U-Pb: 160.9 ± 0.6–154.1 ± 1.2
Maoping	Quartz vein-type and greisen-type W-Sn	Re-Os: 156.8 (Zeng et al., 2009)	Tianmenshan	U-Pb: 152 ± 2.6–150.8 ± 1.8 (Liu et al., 2007)
Niuling	Quartz vein-type W	Re-Os: 154.9 ± 4.1 (Feng et al., 2007)	Hongtaoling	U-Pb: 151.4 ± 3.1 (Feng et al., 2007)
Pangushan	Quartz vein-type W-Mo	Re-Os: 158.8–157.75 (Zeng et al., 2011)	Huangsha	U-Pb: 164.8–153.8 (Fang et al., 2014)

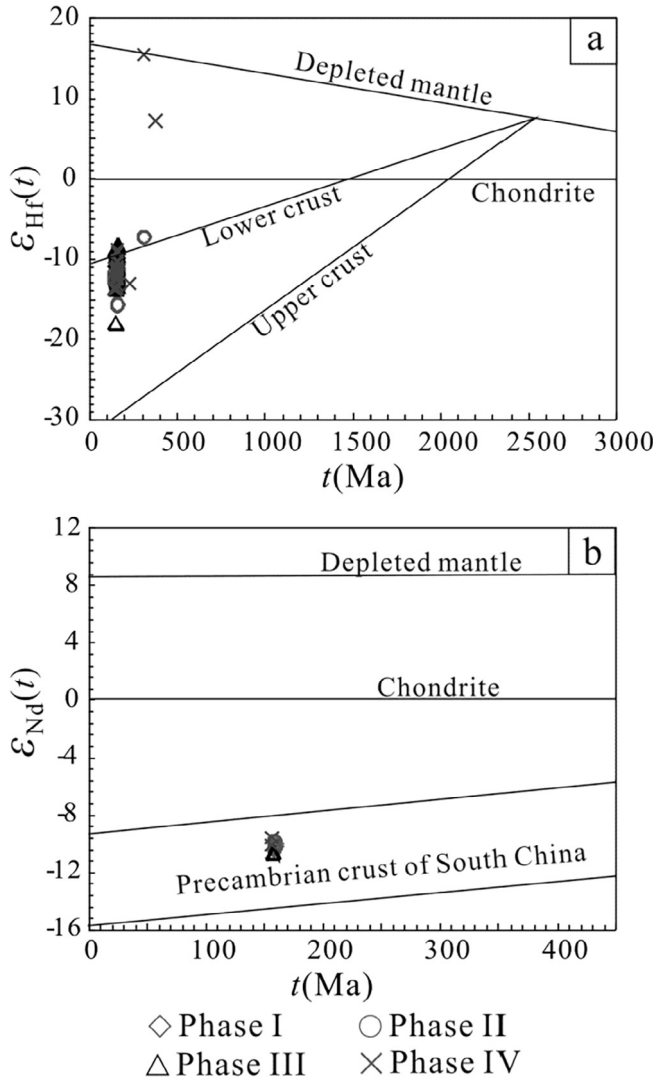

Fig. 12. Various discrimination diagrams for the sources of the Jiulongnao granitic magmas. (a) t vs $\varepsilon_{Hf}(t)$ diagram for zircons; (b) t vs $\varepsilon_{Nd}(t)$ diagram for whole-rocks.

Acknowledgments

This research was funded by grants from the National Key R&D Program of China (No. 2016YFC0600207, 2016YFC0600208), Public Science and Technology Research Funds Projects of MLR, China (No. 201411050) and the National Science Foundation of China (No. 41430314, No. 41372092).

References

Abdel-Rahman, A.F.M., Cuney, M., 1994. Nature of biotites from alkaline, calc-alkaline, and peraluminous magmas. J. Petrol. 35, 1025–1029.

Bali, E., Keppler, H., Audetat, A., 2012. The mobility of W and Mo in subduction zone fluids and the Mo-W-Th-U systematics of island arc magmas. Earth Planet. Sci. Lett. 351–352, 195–207.

Belkasmi, M., Cuney, M., Pollard, P.J., Bastoul, A., 2000. Chemistry of the Ta-Nb-Sn-W oxide minerals from the Yichun rare metal granite (SE China): Genetic implications and comparison with Moroccan and French Hercynian examples. Mineral. Mag. 64, 507–523.

Calas, G., 1979. Etude expérimentale du comportement de l'uranium dans les magmas: États d'oxydation et coordinance. Geochim. Cosmochim. Acta 43, 1521–1531.

Candela, P.A., Bouton, S.L., 1990. The influence of oxygen fugacity on tungsten and molybdenum partitioning between silicate melts and ilmenite. Econ. Geol. 85, 633–640.

Chappell, B.W., 1999. Aluminium saturation in I- and S-type granites and the characterization of fractionated haplogranites. Lithos 46, 535–551.

Chappell, B.W., Bryant, C.J., Wyborn, D., 2012. Peraluminous I-type granites. Lithos 153, 142–153.

Chen, Y.C., Pei, R.F., Zhang, H.L., Lin, X.D., Bai, G., Li, C.Y., Hu, Y.J., Liu, G.Q., Xian, B.Q., 1989. The Geology of Non-Ferrous and Rare Metal Deposits Related to Mesozoic Granitoids in Nanling Region. Geological Publishing House, Beijing.

Chen, Y.X., Li, H., Sun, W.D., Ireland, T., Tian, X.F., Hu, Y.B., Yang, W.B., Chen, C., Xu, D.R., 2016. Generation of Late Mesozoic Qianlishan A_2-type granite in Nanling Range, South China: implications for Shizhuyuan W-Sn mineralization and tectonic evolution. Lithos 266, 435–452.

Fang, G.C., Chen, Y.C., Chen, Z.H., Zeng, Z.L., Zhang, Y.Z., Tong, Q.Q., Sun, J., Huang, H.X., Guo, N.X., 2014. Zircon U-Pb and molybdenite Re-Os geochronology of the Pangushan tungsten deposit in south Jiangxi Province and its significance. Acta Geosci. Sin. 35, 76–84.

Faure, M., Chen, Y., Feng, Z.H., Shu, L.S., Xu, Z.Q., 2017. Tectonics and geodynamics of South China: an introductory note. J. Asian Earth Sci. 141, 1–6.

Feng, C.Y., Huang, F., Zeng, Z.L., Qu, W.J., Ding, M., 2011a. Isotopic chronology of Jiulongnao granite and Hongshuizhai greisens-type tungsten deposit in south Jiangxi Province. J. Jilin Univ. (Earth Sci. Ed.) 41, 111–121.

Feng, C.Y., Xu, J.X., Zeng, Z.L., Zhang, D.Q., Qu, W.J., She, H.Q., Li, J.W., Li, D.X., Du, A.D., Dong, Y.J., 2007. Zircon SHRIMP U-Pb and molybdenite Re-Os dating in Tianmenshan-Hongtaoling tungsten-tin orefield, southern Jiangxi Province, China, and its geological implication. Acta Geol. Sin. 81, 952–963.

Feng, C.Y., Zeng, Z.L., Zhang, D.Q., Qu, W.J., Du, A.D., Li, D.X., She, H.Q., 2011b. SHRIMP zircon U-Pb and molybdenite Re-Os isotopic dating of the tungsten deposits in the Tianmenshan-Hongtaoling W-Sn orefield, southern Jiangxi Province, China, and geological implications. Ore Geol. Rev. 43, 8–25.

Gilder, S.A., Keller, G.R., Luo, M., Goodell, P.C., 1991. Eastern Asia and the Western Pacific timing and spatial distribution of rifting in China. Tectonophysics 197, 225–243.

Guo, C.L., 2010. Study on Mineralization-Related Mesozoic Granitoids in Chongyi-Shangyou Counties, South Jiangxi, and Comparison to Corresponding Granitoids in the Nanling Region, South China. Chinese Academy of Geological Sciences, Beijing.

Guo, C.L., Chen, Y.C., Li, C.B., Chen, Z.H., Lou, F.S., 2011a. Zircon SHRIMP U-Pb dating, geochemistry, Sr-Nd isotopic analysis of the late Jurassic granitoids in the Jiulongnao W-Sn-Pb-Zn ore-concentrated areas in Jiangxi Province and their geological significance. Acta Geol. Sin. 85, 1188–1205.

Guo, C.L., Chen, Y.C., Zeng, Z.L., Lou, F.S., 2012. Petrogenesis of the Xihuashan granites in southeastern China: Constraints from geochemistry and in-situ analyses of zircon U-Pb-Hf-O isotopes. Lithos 148, 209–227.

Guo, C.L., Mao, J.W., Bierlein, F., Chen, Z.H., Chen, Y.C., Li, C.B., Zeng, Z.L., 2011b. SHRIMP U-Pb (zircon), Ar-Ar (muscovite) and Re-Os (molybdenite) isotopic dating of the Taoxikeng tungsten deposit, South China Block. Ore Geol. Rev. 43, 26–39.

Guo, N.X., Lü, X.Q., Zhao, Z., Chen, Z.Y., 2014. Petrological and mineralogical characteristics of two types of metallogenic granitoid formed during the Mesozoic Period, Nanling region. Acta Geol. Sin. 88, 2423–2436.

Guo, N.X., Wang, D.H., Zhao, Z., Chen, Y.C., Chen, W., Xie, X.W., 2017. Mineral characteristics of the Jiulongnao granite batholith in southern Jiangxi Province and its indication of magma evolution and mineralization. Earth Sci. Front. 24, 76–92.

He, X.X., Tang, S.H., Zhu, X.K., Wang, J.H., 2007. Precise measurement of Nd isotopic ratios by means of multi-collector magnetic sector inductively coupled plasma mass spectrometry. Acta Geosci. Sin. 28, 405–410.

Henry, D.J., Guidotti, C.V., Thomson, J.A., 2005. The Ti-saturation surface for low-to-medium pressure metapelitic biotites: Implications for geothermometry and Ti-substitution mechanisms. Am. Mineral. 90, 316–328.

Hou, K.J., Li, Y.H., Zou, T.R., Qu, X.M., Shi, Y.R., Xie, G.Q., 2007. Laser ablation-MC-ICP-MS technique for Hf isotope microanalysis of zircon and its geological applications. Acta Petrol. Sin. 23, 2595–2604.

Hou, K.J., Tian, Y.R., Li, Y.H., 2009. In situ U-Pb zircon dating using laser ablation-multi ion counting-ICP-MS. Mineral. Deposits 28, 481–492.

Hu, R.Z., Chen, W.T., Xu, D.R., Zhou, M.F., 2017. Reviews and new metallogenic models of mineral deposits in South China: an introduction. J. Asian Earth Sci. 137, 1–8.

Ji, W.B., Lin, W., Faure, M., Chen, Y., Chu, Y., Xue, Z.H., 2017. Origin of the Late Jurassic to Early Cretaceous peraluminous granitoids in the northeastern Hunan province (middle Yangtze region), South China: Geodynamic implications for the Paleo-Pacific subduction. J. Asian Earth Sci. 141, 174–193.

Lee, C.T., Luffi, P., Le, R.V., Dasgupta, R., Albaréde, F., Leeman, W.P., 2010. The redox state of arc mantle using Zn/Fe systematics. Nature 468, 681–685.

Legros, H., Marignac, C., Mercadier, J., Cuney, M., Richard, A., Wang, R.C., Charles, N., Lespinasse, M.Y., 2016. Detailed paragenesis and Li-mica compositions as recorders of the magmatic-hydrothermal evolution of the Maoping W-Sn deposit (Jiangxi, China). Lithos 264, 108–124.

Li, G.L., Hua, R.M., Wei, X.L., Qu, W.J., Huang, X.E., Hu, D.Q., Zhou, L.Q., 2014. Re-Os isotoic ages of two types of molybdenite from Zhangdongkeng tungsten deposit in southern Jiangxi Province and their geologic implications. Earth Sci. 39, 165–173.

Li, X.H., Liu, D.Y., Sun, M., Li, W.X., Liang, X.R., Liu, Y., 2004. Precise Sm-Nd and U-Pb isotopic dating of the supergiant Shizhuyuan polymetallic deposit and its host granite, SE China. Geol. Mag. 141, 225–231.

Liu, S.B., Wang, D.H., Chen, Y.C., Xu, J.X., Zeng, Z.L., Ying, L.J., Wang, C.H., 2007. SHRIMP dating of Tianmenshan granite pluton and granite-porphyry dyke in southern Jiangxi Province, eastern Nanling region, and its significance. Acta Geol. Sin. 81, 972–978.

Liu, X.C., Xing, H.L., Zhang, D.H., 2015. The mechanisms of the infill textures and its implications for the five-floor zonation at the Dajishan vein-type tungsten deposit, China. Ore Geol. Rev. 65, 365–374.

Liu, X.C., Xing, H.L., Zhang, D.H., 2017. The mechanisms and time scale of alteration halos in vein-type tungsten deposits in southern China. Ore Geol. Rev. 89, 1019–1029.

Liu, Y.S., Gao, S., Hu, Z.C., Gao, C.G., Zong, K.Q., Wang, D.B., 2010. Continental and

oceanic crust recycling-induced melt-peridotite interactions in the Trans-North China Orogen: U-Pb dating, Hf isotopes and trace elements in zircons from mantle xenoliths. J. Petrol. 51, 537–571.
Liu, Y.S., Hu, Z.C., Gao, S., Günther, D., Xu, J., Gao, C.G., Chen, H.H., 2008. In situ analysis of major and trace elements of anhydrous minerals by LA-ICP-MS without applying an internal standard. Chem. Geol. 257, 34–43.
Ludwig, K.R., 2003. Users manual for Isoplot/Ex: A geochronological toolkit for Microsoft Excel 1a.
Lumpkin, G.R., Chakoumakos, B.C., Ewing, R.C., 1986. Mineralogy and radiation effects of microlite from the Harding pegmatite, Taos County, New Mexico. Am. Mineral. 71, 569–588.
Mao, J.W., Pirajno, F., Cook, N., 2011. Mesozoic metallogeny in East China and corresponding geodynamic settings — An introduction to the special issue. Ore Geol. Rev. 43, 1–7.
Miller, C.F., McDowell, S.M., Mapes, R.W., 2003. Hot and cold granites? Implications of zircon saturation temperatures and preservation of inheritance. Geology 31, 529–532.
Mungall, J.E., 2002. Roasting the mantle: Slab melting and the genesis of major Au and Au-rich Cu deposits. Geology 30, 915.
Nakada, S., Takahashi, M., 1979. Regional variation in chemistry of the Miocene intermediate to felsic magmas in the Outer Zone and the Setouchi Province of Southwest Japan. J. Geol. Soc. Jpn. 85, 571–582.
Oyarzun, R., Márquez, A., Lillo, J., López, I., Rivera, S., 2001. Giant versus small porphyry copper deposits of Cenozoic age in northern Chile: Adakitic versus normal calc-alkaline magmatism. Miner. Deposita 36, 794–798.
Panina, L.I., Rokosova, E.Y., Isakova, A.T., Tolstov, A.V., 2017. Mineral composition of alkaline lamprophyres of the Tomtor massif as reflection of their genesis. Russ. Geol. Geophys. 58, 887–902.
Peccerillo, A., Taylor, S.R., 1976. Geochemistry of Eocene calc-alkaline volcanic rocks from the Kastamonu area, Northern Turkey. Contrib. Miner. Petrol. 58, 63–81.
Pichavant, M., Hammouda, T., Scaillet, B., 1996. Control of redox state and Sr isotopic composition of granitic magmas: a critical evaluation of the role of source rocks. In: Brown, M., Candela, P.A., Peck, D.L., Stephens, W.E., Walker, R.J., Zen, E. (Eds.), The Third Hutton Symposium on the Origin of Granites and Related Rocks. Geological Society of America.
Qi, L., Hu, J., Gregoire, D.C., 2000. Determination of trace elements in granites by inductively coupled plasma mass spectrometry. Talanta 51, 507–513.
Robinson, D.M., Miller, C.F., 1999. Record of magma chamber processes preserved in accessory mineral assemblages, Aztec Wash Pluton, Nevada. Am. Mineral. 84, 1346–1353.
Romer, R.L., Kroner, U., 2016. Phanerozoic tin and tungsten mineralization — Tectonic controls on the distribution of enriched protoliths and heat sources for crustal melting. Gondwana Res. 31, 60–95.
Rubatto, D., 2002. Zircon trace element geochemistry: Partitioning with garnet and the link between U-Pb ages and metamorphism. Chem. Geol. 184, 123–138.
Rudnick, R.L., Gao, S., 2013. Composition of the Continental Crust, 2nd ed, Treatise on Geochemistry, second ed. Elsevier Ltd.
Sato, K., 2012. Sedimentary crust and metallogeny of granitoid affinity: implications from the geotectonic histories of the Circum-Japan Sea region, Central Andes and Southeastern Australia. Resour. Geol. 62, 329–351.
Shu, L.S., 2012. An analysis of principal features of tectonic evolution in South China Block. Geol. Bull. China 31, 1035–1053.
Shu, L.S., Zhou, X.M., Deng, P., Yu, X.Q., 2006. Principal geological features of Naling tectonic belt, South China. Geol. Rev. 52, 251–265.
Sláma, J., Košler, J., Condon, D.J., Crowley, J.L., Gerdes, A., Hanchar, J.M., Horstwood, M.S.A., Morris, G.A., Nasdala, L., Norberg, N., 2008. Plešovice zircon — a new natural reference material for U-Pb and Hf isotopic microanalysis. Chem. Geol. 249, 1–35.
Sun, S.S., McDonough, W.F., 1989. Chemical and isotopic systematics of oceanic basalts: implications for mantle composition and processes. Geol. Soc. Lond. Spec. Publ. 42, 313–345.
Sun, W., Arculus, R.J., Kamenetsky, V.S., Binns, R.A., 2004. Release of gold-bearing fluids in convergent margin magmas prompted by magnetite crystallization. Nature 431, 975–978.
Tan, Y.J., 1984. Composition characteristics of garnet in granitoids. Earth Environ. 6, 20–26.
Tang, A., Li, G.L., Zhou, L.Q., Su, H., Tong, K.Y., 2016. Geological characteristics of micas with zonal structure in pegmatite from Maoping tungsten deposit and its significance to magma-fluid evolution process, southern Jiangxi. Geol. Sci. Technol. Inform. 35, 30–37.
Trail, D., Watson, E.B., Tailby, N.D., 2012. Ce and Eu anomalies in zircon as proxies for the oxidation state of magmas. Geochim. Cosmochim. Acta 97, 70–87.
Wang, D.H., Chen, Y.C., Chen, Z.H., Liu, S.B., Xu, J.X., Zhang, J.J., Zeng, Z.L., Chen, F.W., Li, H.Q., Guo, C.L., 2007. Assessment on mineral resource in Nanling region and suggestion for further prospecting. Acta Geol. Sin. 81, 882–890.
Wang, D.H., Zhao, Z., Liu, S.B., Guo, N.X., Liang, T., Chen, W., Zhou, X.P., 2016. Patterns of metallogenesis of Jiulongnao orefield in the east section of the Nanling region and direction for prospecting. Acta Geol. Sin. 90, 2399–2411.
Wang, F.Y., Li, C.Y., Ling, M.X., Zhang, H., Sun, Y.L., Sun, W.D., 2011. Geochronology of the Xihuashan tungsten deposit in southeastern China: constraints from Re-Os and U-Pb dating. Resour. Geol. 61, 414–423.
Wang, H.Y., Zhao, Z., Wang, D.H., Guo, N.X., Chen, Z.Y., Hou, K.J., Li, C., Zhou, H., Chen, W., 2017a. Geological characteristics, rock forming and ore-forming age and prospecting of Meishuping tungsten-molybdenum deposit in JiangXi. Earth Sci. Front. 24, 109–119.
Wang, R.C., Fontan, F., Chen, X.M., Hu, H., Liu, C.S., Xu, S.J., Parseval, P.D., 2003. Accessory minerals in the Xihuashan Y-enriched granitic complex, southern China: a record of magmatic and hydrothermal stages of evolution. Can. Mineral. 41, 727–748.
Wang, R.C., Wang, D.Z., Zhao, G.T., Lu, J.J., Chen, X.M., Xu, S.J., 2001. Accessory mineral record of magma-fluid interaction in the Laoshan I- and A-type granitic complex, Eastern China. Phys. Chem. Earth Part A 26, 835–849.
Wang, R.C., Yu, A.P., Chen, J., Xie, L., Lu, J.J., Zhu, J.C., 2012. Cassiterite exsolution with ilmenite lamellae in magnetite from the Huashan metaluminous tin granite in southern China. Mineral. Petrol. 105, 71–84.
Wang, R.C., Zhu, J.C., Zhang, W.L., Lei, X., Yu, A.P., Che, Y.D., 2008. Ore-forming mineralogy of W-Sn granites in the Nanling Range: concept and case study. Geol. J. China Univ. 14, 485–495.
Wang, S.Y., Zhao, Z., Fang, G.C., Wang, D.H., Guo, N.X., Ouyang, X., Chen, Z.Y., Hou, K.J., 2017b. Mineralogical and geochronological characteristics of the Zhang (dongkeng)-Jiu (longnao) tungsten polymetallic deposit, southern Jiangxi Province, and its geological implications. Earth Sci. Front. 24, 120–130.
Watson, E.B., Harrison, T.M., 1983. Zircon saturation revisited: temperature and composition effects in a variety of crustal magma types. Earth Planet. Sci. Lett. 64, 295–304.
Whalen, J.B., Chappell, B.W., 1988. Opaque mineralogy and mafic mineral chemistry of I- and S-type granites of the Lachlan fold belt, southeast Australia. Am. Mineral. 73, 281–296.
Wones, D.R., Eugster, H.P., 1965. Stability of biotite: experiment, theory, and application. Am. Mineral. 50, 1228–1272.
Wu, F.Y., Sun, D.Y., Li, H.M., Jahn, B., Wilde, S., 2002. A-type granites in northeastern China: age and geochemical constraints on their petrogenesis. Chem. Geol. 187, 143–173.
Xiang, Y.X., Yang, J.H., Chen, J.Y., Zhang, Y., 2017. Petrogenesis of Lingshan highly fractionated granites in the Southeast China: implication for Nb-Ta mineralization. Ore Geol. Rev. 89, 495–525.
Yang, J.H., Peng, J.T., Hu, R.Z., Bi, X.W., Zhao, J.H., Fu, Y.Z., Shen, N.P., 2013. Garnet geochemistry of tungsten-mineralized Xihuashan granites in South China. Lithos 177, 79–90.
Yang, L.Q., Deng, J., Dilek, Y., Meng, J.Y., Gao, X., Santosh, M., Wang, D., Yan, H., 2016. Melt source and evolution of I-type granitoids in the SE Tibetan Plateau: late Cretaceous magmatism and mineralization driven by collision-induced transtensional tectonics. Lithos 245, 258–273.
Yang, M.G., Mei, Y.W., Zhou, Z.Y., Rui, B., Zhan, M.G., Tong, Q.M., Feng, Z.W., Liu, X., Yang, E.Z., 1998. Ore-Forming Regularities and Ore-Searching Prediction of Luoxiao-Wuyi Uplift and Chenzhou-Shangrao Depression. Geological Publishing House, Beijing.
Yin, J.W., Kim, S.J., Lee, H.K., Itay, T., 2002. K-Ar ages of plutonism and mineralization at the Shizhuyuan W-Sn-Bi-Mo deposit, Hunan Province, China. J. Asian Earth Sci. 20, 151–155.
Zeng, Z.L., Zhang, Y.Z., Zhu, X.P., 2009. Re-Os isotopic dating of molybdenite from the Maoping tungsten-tin deposit in Chongyi County of Southern Jiangxi province and its geological significance. Rock Mineral. Anal. 28, 209–214.
Zeng, Z.L., Zhang, Y.Z., Chen, Z.H., Chen, Y.C., Zhu, X.P., Tong, Q.Q., Zheng, B.H., Zhou, Y., 2011. Geological characteristics and metallogenic epoch of Pangushan W-Bi(Te) ore deposit in Yudu County, Jiangxi province. Mineral. Deposits 30, 949–958.
Zhao, K.D., Jiang, S.Y., Jiang, Y.H., Wang, R.C., 2005. Mineral chemistry of the Qitianling granitoid and the Furong tin ore deposit in Hunan Province, South China: implication for the genesis of granite and related tin mineralization. Eur. J. Mineral. 17, 635–648.
Zhao, W.W., Zhou, M.F., Li, Y.H.M., Zhao, Z., Gao, J.F., 2017a. Genetic types, mineralization styles, and geodynamic settings of Mesozoic tungsten deposits in South China. J. Asian Earth Sci. 137, 109–140.
Zhao, Z., Wang, D.H., Chen, Y.C., Liu, S.B., Fang, G.C., Liang, T., Guo, N.X., Wang, S.Y., Wang, H.Y., Liu, Z.Q., Zeng, Z.L., Ding, M., Chen, W., Zhou, X.P., 2017b. "Patterns of metallogenesis of Jiulongnao" and demonstration of the deep prospecting: the expansion of "Five levels + basement" exploration model. Earth Sci. Front. 24, 8–16.
Zhou, X.M., Li, W.X., 2000. Origin of Late Mesozoic igneous rocks in southeastern China: implications for lithosphere subduction and underplating of mafic magmas. Tectonophysics 326, 269–287.
Zhou, X.M., Sun, T., Shen, W.Z., Shu, L.S., Niu, Y.L., 2006. Petrogenesis of Mesozoic granitoids and volcanic rocks in South China: a response to tectonic evolution. Episodes 29, 26–33.